Muon g-2 storage ring beam and spin dynamics

Editors: J. D. Crnkovic,[1,*] D. W. Hertzog,[2] W. M. Morse,[1] and D. Stratakis[3]
(Muon $g-2$ Collaboration)
[1] *Brookhaven National Laboratory, Upton, New York 11973-5000, USA*
[2] *Department of Physics, University of Washington, Seattle, Washington 98195-1560, USA*
[3] *Fermi National Accelerator Laboratory, Batavia Illinois 60510-5011, USA*
(Dated: January 27, 2020)

Jason

The Fermilab Muon $g-2$ Experiment is currently collecting and analyzing data, where it has the goals of measuring the muon anomaly with 140 parts-per-billion (ppb) precision and electric dipole moment with at least 100 times more sensitivity than the previous measurement. The Fermilab experiment uses the refurbished and upgraded BNL Muon $g-2$ storage ring system, where these high precision measurements require a detailed understanding of the muon storage ring beam and spin dynamics for determining systematic corrections and uncertainties. The scintillating-fiber beam monitor, straw tracker, and calorimeter systems provide information about the storage ring beam, and detailed measurements and models of the storage ring guide fields have also been produced. The following discussion provides an overview of the Muon $g-2$ storage ring beam and spin dynamics, along with the associated systematic effects.

CONTENTS

I. Introduction 1

II. Experimental Method 2
A. Polarized Muon Production 2
B. Spin Precession 2
C. Magnetic Field 4

III. Storage Ring 5

IV. Simulation Tools 7
A. G4beamline 7
B. Phase Space Models 7
C. Bmad 7
1. Quadrupoles 8
2. Main Magnet 8
3. Injection Channel 8
D. COSY INFINITY 8
E. gm2ringsim 9

V. Storage Ring Optics 9
A. Injection 11
B. Average Tune & Chromaticity Measurements 11
C. Closed Orbit & Quadrupole Distortions 16

VI. Systematics 17
A. Coherent Beam Motion & Detector Acceptance 18
B. Pitch Correction 22
C. E-field Correction 22
D. Spin Correlations & Early-to-late Effects 23
E. Spin Resonances 25
F. Lost Muons 25

VII. Conclusion 26

Acknowledgments 27

A. An Appendix 27
1. An Appendix Subsection 27

References 27

I. INTRODUCTION

Jason

Muon dipole moment measurements [1–4] provide an important test of the Standard Model (SM), where the Brookhaven National Laboratory (BNL) Muon $g-2$ Experiment is the last completed experiment in a series of muon anomaly (a_μ) and electric dipole moment (d_μ) measurements. The Fermi National Accelerator Laboratory (Fermilab) Muon $g-2$ Experiment [5] is currently collecting and analyzing data, where it has completed the first physics data taking run (Run-1) and is now in the second physics data taking run (Run-2).

The Fermilab experiment can calculate a_μ from [5]

$$a_\mu = \left(\frac{g_e}{2}\frac{m_\mu}{m_e}\frac{\omega_a}{\langle\omega_p\rangle}\right)\Big/\left(\frac{\mu_e}{\mu_p}\right), \tag{1}$$

where g_e is the electron g-factor, m_μ/m_e is the muon-electron mass ratio, ω_a is the anomalous precession frequency, and μ_e/μ_p is the electron-proton magnetic moment ratio. The $\langle\omega_p\rangle$ in Eq. (1) corresponds to the average magnetic field seen by the muons, where the field has been written in terms of the corresponding free proton Larmor frequency because pulsed nuclear magnetic

* jcrnkovic@bnl.gov

DRAFT

resonance (NMR) is used to measure the field. Values for g_e, m_μ/m_e, and μ_e/μ_p can be obtained from CODATA [6], where these quantities have relative uncertainties of 0.000 26, 22, and 3.0 ppb respectively. The Fermilab experiment will measure ω_a and $\langle\omega_p\rangle$ to calculate the corresponding a_μ.

The final BNL a_μ value [7] has a relative statistical and systematic precision of 460 and 280 parts-per-billion (ppb) receptively, for a total precision of 540 ppb when adding the two uncertainties in quadrature. There is a greater than $3\,\sigma$ difference between the BNL measurement and SM prediction [7], which hints at the possibility of physics beyond the SM. The Fermilab experiment has the goal of measuring a_μ with a final statistical and systematic precision of 100 ppb respectively, for a total precision of 140 ppb when adding the two uncertainties in quadrature. The 100 ppb statistical uncertainty is for ω_a, as the statistical uncertainty for $\langle\omega_p\rangle$ is negligible, and the ω_a and $\langle\omega_p\rangle$ measurements are to each have a 70 ppb systematic precision. The BNL $|d_\mu| < 1.8\times10^{-19}\,e\,\mathrm{cm}$ (95 % C.L.) measurement provides a factor of 5 improvement in sensitivity with respect to the previous limit, and the Fermilab experiment has the goal improving the sensitivity by at least a 100 times with respect to the BNL measurement.

Achieving a 70 ppb systematic precision for ω_a requires a detailed understanding of the muon storage ring beam and spin dynamics. The Fermilab experiment uses the refurbished and upgraded BNL muon storage ring system, where the following discussion describes the storage ring magnetic and electric guide fields, lattice functions, tunes, closed orbits, polarized muon injection, and storage of the muons. The scintillating-fiber beam monitor (FBM), straw tracker, and calorimeter systems are also discussed, as these systems provide information about the storage ring beam. Finally, an overview of the known ω_a systematic effects that arise from beam and spin dynamics is also given.

II. EXPERIMENTAL METHOD

A. Polarized Muon Production

Diktys

A combination of beamlines that are part of the so-called Muon Campus [8] have been designed [9] and commissioned [10] to deliver an intense polarized muon beam for the Fermilab Muon $g-2$ Experiment. A schematic layout of this facility is illustrated in Fig. 1. Protons accelerated in the upgraded Fermilab linac and booster synchrotron [11] are adiabatically re-bunched [12] in the recycler synchrotron for the Fermilab Muon Campus operations, and then the 8 GeV proton bunches are directed to an Inconel-600 (nickel-iron alloy) target [13] via the M1-line. A secondary beam from the target is collected using a lithium lens, where the positively charged particles with 3.1 GeV/c (±10 %) are selected by using a bending magnet. The secondary beam leaves the target station and travels through the M2- and M3-line, which are designed to capture as many 3.1 GeV/c muons as possible from the pion decays.

Positive pion decays produce positive muons and muon neutrinos: $\pi^+ \to \mu^+ + \nu_\mu$. In the pion rest-frame, the pion has zero spin and the neutrino is left-handed, and so the muon is also left-handed to conserve angular momentum. When the muon has a pion rest-frame momentum parallel to the lab-frame pion momentum (forward decay), then the Lorentz boost will produce a higher momentum left-handed muon in the lab-frame. When the muon has a pion rest-frame momentum antiparallel to the lab-frame pion momentum (backward decay), then the Lorentz boost will produce a lower momentum right-handed muon in the lab-frame. A beam with ~95 % polarization is obtained for the Muon $g-2$ Experiment by selecting the higher momentum muons in the lab-frame.

The beam is then injected into the Delivery Ring (DR), where the majority of the remaining pions decay into muons after several revolutions. The DR is also used to separate muons in time from the heavier protons, and a kicker is then used to remove the protons, where the muon beam is extracted into the M4-line. Injection from the M3-line and extraction to the M4-line takes place in the same straight section with the latter happening in the downstream half. The 128.0 m long M4-M5-line transfers the beam from the DR towards the Muon g–2 storage ring located in the MC-1 Hall. The M5-line includes a 27.1° horizontal bend string that provides the proper entry position and angle into the storage ring, and right before the end of the M5-line there is a strong-focusing and tunable final focus section, using four quadrupole magnets that provide optical matching to the muon storage ring.

B. Spin Precession

Jason

Elaborate on the spin precession.

The magnetic ($\vec{\mu}$) dipole moment for a fermion is given by

$$\vec{\mu} = g\frac{q}{2m}\vec{s},$$

where g is the dimensionless g-factor, q is charge, m is mass, and $\vec{s}$ is spin. Dirac theory predicts $g = 2$ for spin-1/2 point particles such as the muon, while Standard Model (SM) quantum field theory predicts $g \neq 2$. The deviation of g from 2 is given by the anomaly: $a \equiv (g-2)/2$. The longitudinal component of $\vec{s}$ relative to the particle momentum ($\vec{p}$) is given by [**?**],

$$\frac{d}{dt}(\vec{s}\cdot\hat{p}) = -\frac{q}{m}\left[\vec{s}-(\vec{s}\cdot\hat{p})\,\hat{p}\right]\cdot \left\{a\hat{p}\times\vec{B}+\left[(1+a)\frac{p}{mc\gamma}-\frac{mc\gamma}{p}\right]\frac{\vec{E}}{c}\right\}, \quad (2)$$

DRAFT

FIG. 1: Diktys A diagram of the Muon Campus accelerator complex that is used by the Muon $g-2$ Experiment. *Trying to get a less pixelated image from Brian Drendel or Lee.*

where t is time, $\vec{B}$ is the magnetic field, γ is the Lorentz factor, c is the speed of light, and $\vec{E}$ is the electric field.

The experiment works by injecting a polarized muon beam from the Fermilab Muon Campus [9] into the circular muon storage ring and measuring the arrival time and energy of the corresponding decay positrons with 24 calorimeters [14, 15] placed uniformly around the inside of the ring. Decay positron arrival time, energy, and trajectory are also measured at 2 locations in the storage ring with straw-tracker stations [5] placed inside of the vacuum chamber system. A modulation on top of the muon exponential decay is observed in the decay positron time spectrum after applying a suitable energy threshold cut to the positron events:

$$n(t) = N(t)\, e^{-t/\tau} \left\{1 - A(t) \cos\left[\omega_a t + \phi(t)\right]\right\}, \qquad (3)$$

where N is the normalization, $\tau \sim 64.44\,\mu\text{s}$ is the average lab-frame muon lifetime, A is the asymmetry, $\omega_a \sim 1.439\,\text{rad}/\mu\text{s}$ *[check values]* is the anomalous spin precession frequency, and ϕ is the so called "$g-2$ phase". The N, A, and ϕ terms in Eq. 3 depend on the decay positron energy (E_p) threshold cut value (E_{th}): $E_p \geq E_{\text{th}}$. The E_{th} is typically chosen to be $\sim$1.8 GeV. The N, A, and ϕ terms also depend on time due to the coherent beam motion inside of the storage ring and detector acceptance effects, see Section VI A.

The BNL and Fermilab experiments are sensitive to $\vec{s} \cdot \hat{p}$, where ω_a is the angular frequency at which the muon $\vec{s}$ rotates with respect to $\vec{p}$ and ω_a can be obtained from solutions to Eq. (2).

The experimental method is to circulate a beam of polarized muons in a storage ring and to measure the precession frequency, or rather the difference between the precession frequency and the revolution frequency, ω_a, the spin tune. The 3.094 GeV/c momentum muons decay with lifetime of about 64 µs in the lab frame to a positron and a pair of neutrinos. The energy of the positron in the lab frame is correlated with the polarization of the parent muon. The variation in the number of high energy positrons with time is the measure of ω_a.

The frequency with which the muons precess depends on the details of the magnetic and electric guide field of the storage ring. Magnetic focusing is evidently precluded as it would introduce an unacceptable variation in the magnetic field across the storage region. Instead vertical focusing is provided by electrostatic quadrupoles. The muon momentum is chosen to minimize the effect of the electric field on the precession frequency. Indeed, at the muon magic momentum, 3.094 GeV/c, the contribution of the electric field to the difference frequency vanishes.

Muons decay to $\mu^+ \to e^+ + \bar{\nu}_\mu + \nu_e$. The muon spin is correlated with the momentum of the electron in the lab frame. In the muon rest frame the spin is in the z direction. The total final state momentum is the sum of neutrinos and positron. The max momentum of the final state positron is when neutrinos have the same momentum (same direction) and the positron has equal but opposite. Since the spin of the neutrinos is equal but opposite, the positron carries off the angular momentum of the muon. The e^+, an anti-lepton is most likely to be right handed in a weak decay, and therefore with momentum in the same direction as that of the muon spin. The positron with minimum momentum in the muon rest frame will be when neutrinos are in opposite directions, with total spin 1 and the positron has near zero momentum and the spin opposite that of the muon. It is as before most likely to be right handed, and therefore to

Preliminary
DRAFT

have momentum opposite to the muon spin. The result is that in the lab frame, positron momenta is correlated with muon spin. The measurement is by counting the time dependence of the number of high momentum decay positrons. The experiment is equipped with calorimeters that measure the number vs time of high momentum positrons. The muon has equal but opposite momentum to the neutrinos and necessarily the muon spin. The detector acceptance depends on the transverse position of the decay muon. Therefore acceptance varies with the betatron and dispersive variation of the distribution in phase space of the muon beam.

Momentum of the positron is correlated with the muon spin. Measurement of decay positron momentum as function of time is precession frequency. Focusing is the dipole field and electrostatic quads. So as not to introduce a field variation. But the E-field couples to the magnetic moment anyway. If the dimensionless g-factor of the muon were identically 2, then in any magnetic field the spin will stay synched with the trajectory independent of its momentum. In an electric field, if $g = 2$, then at $\beta \ll 1$ there is no effect on the polarization and polarization is fixed independent of trajectory. At $\gamma \gg 1$ the magnetic field in the rest frame of the muon is $B \to cE$ and the spin is again pinned to the trajectory. Since $g > 2$ the spin rotates more rapidly than the trajectory. There is a momentum, the so-called magic momentum, where the spin follows the trajectory. And for the muon that is at $\gamma = 29.3$. The spin is frozen to the direction in an electric field. By operating at the magic momentum, the E-field the precession is decoupled from the E-field.

The expression for the anomalous precession frequency, in the limit of vanishing longitudinal magnetic field, is

$$\vec{\omega}_a = -\frac{q}{m}\left[a_\mu \vec{B} - a_\mu\left(\frac{\gamma}{\gamma+1}\right)\left(\vec{\beta}\cdot\vec{B}\right) - \left(a_\mu - \frac{1}{\gamma^2-1}\right)\frac{\vec{\beta}\times\vec{E}}{c}\right]. \tag{4}$$

For muons at magic momentum,

$$p_0 = \frac{mc}{\sqrt{a_\mu}},$$

circulating on the design orbit,

$$\vec{\omega}_a = -\frac{q}{m} a_\mu \vec{B}.$$

C. Magnetic Field

Jason

When a free spin-1/2 proton is placed in an external magnetic field, then it will have eigenstates separated by the following energy difference (ΔE):

$$\omega_p = \gamma_p B$$
$$\Delta E = \hbar\omega_p. \tag{5}$$

TABLE I: Jason Muon $g-2$ storage ring magnet parameters [3] *[Do any of these values need updating???]*.

Parameter	Value
Nominal Magnetic Field	1.4513 T
Nominal Current	5200 A
Central Orbit (Magic) Radius	7112 mm
Muon Storage Region Radius	45 mm
Magnet Gap Length	180 mm
Nominal Stored Energy	6 MJ

Equation (5) depends on the free proton Larmor frequency (ω_p), free proton gyromagnetic ratio ($\gamma_p = 2\pi$ rad/cycle $\times$ 42.577 478 92(29) MHz/T [6]), magnitude of the external magnetic field (B), and reduced Planck constant ($\hbar$). Pulsed NMR is used to measure the storage ring magnetic field [3, 5, 16], where it works by exciting protons in a magnetic field with a radio frequency (RF) pulse and then measuring the resulting RF signal that is generated by the protons relaxing back into the equilibrium state. The resulting RF signal can be analyzed to extract the corresponding shielded proton Larmor frequency. The pulsed NMR probes are based on water or petroleum jelly, where internal diamagnetic shielding of the molecular protons must be corrected for to obtain the corresponding ω_p in Eq. (5).

Achieving a 70 ppb systematic precision for $\langle\omega_p\rangle$ requires a very uniform magnetic field in the storage region of the ring, where Table I gives selected Muon g–2 storage ring magnet parameters. The storage region is effectively defined by 5 circular collimators that are used to scape the muon beam before the measurement period, see Section VI F. The storage region is a torus centered on the storage ring central orbit that has a circular cross section radius of 45 mm and a central circumference of 44 690 mm that corresponds to a region of 2.8×10^8 mm^3. The Fermilab experiment uses passive and active shimming to produce the very uniform storage region magnetic field, where the specifications are that the field vary by less than 1 ppm over the 45 mm cross section radius and individual multipole contributions vary by less than 1 ppm when averaged over the azimuth (angular displacement along the storage ring central orbit) [5]. The experiment also has the goal of trying to reduce these individual multipole variations to 100 ppb [5]. *Verify field specs/goals with one of the g–2 field experts.* The storage region magnetic field is averaged over the run time and muon beam x-y-profile (obtained from straw tracker system measurements) to obtain $\langle\omega_p\rangle$.

If the beam of charged particles is ignored, then there should be no free currents inside of the storage region. Hence, a magnetic scalar potential (ϕ_B), which satisfies Laplace's equation, can be used to approximate the magnetic field ($\vec{B} = -\vec{\nabla}\phi_B$) inside of the storage region. A multipole expansion can be used to parametrize the transverse magnetic field components when considering

DRAFT

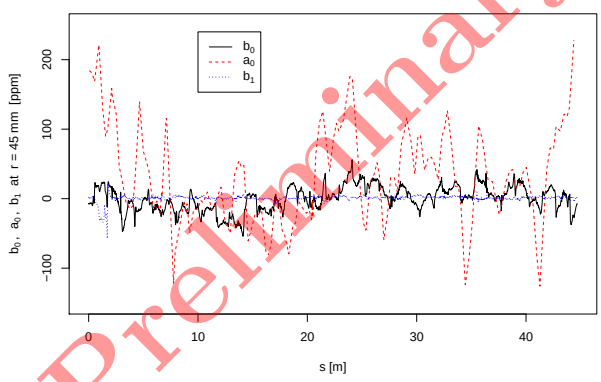

FIG. 2: Mike Preliminary storage ring magnetic field measurement data. Deviations from the main dipole field component in the vertical (b_0) and radial (a_0) directions in parts per million are indicated, as well as the normal quadrupole gradient (b_1) in parts per million at a displacement of 45 mm from the central orbit. *Harmonize notation; check with field & tracker experts.*

a cross section slice of the storage region,

$$B_x(r,\theta) = \sum_{n=0}^{\infty} \left(\frac{r}{r_0}\right)^n \left[-b_n \cos(n\theta) + a_n \sin(n\theta)\right]$$
$$B_y(r,\theta) = \sum_{n=0}^{\infty} \left(\frac{r}{r_0}\right)^n \left[a_n \cos(n\theta) + b_n \sin(n\theta)\right], \quad (6)$$

where a_0 is the constant term and r_0 is the radius at which the normal (a_n) and skew (b_n) multipole coefficients are normalized *[verify skew-normal convention being used by $g-2$ field experts]*. Equation (6) can also be used to parameterize the field measurements after the data has been averaged over the azimuth. The r and θ in Eq. (6) are the radial and angular polar coordinates respectively, where $r = 0$ corresponds to the central orbit and $\theta = 0$ corresponds to the radially outward direction of the storage ring. Furthermore, the storage ring horizontal (radial) and vertical transverse coordinates can be written as $x = r\cos(\theta)$ and $y = r\sin(\theta)$ respectively. Figure 2 shows normal dipole, skew dipole, and normal quadrupole coefficients for preliminary magnetic field measurements of the storage region. *The results in Fig. 2 do meet the field spec. Something should be said about this!*

III. STORAGE RING

Renee

Figure 3 shows the layout of the Muon $g-2$ storage ring. Muons are injected into the circular storage ring, which has a 7.112 m central radius (R_0), 44.69 m circumference (C_0), and 0.149 µs revolution period. A 1.4513 T vertical magnetic dipole field [5, 17] provides horizontal (radial) focussing, while an electrostatic quadrupole system [5, 18, 19] provides vertical focusing. The Muon $g-2$ storage ring is a weak focusing machine with a single adjustable parameter, namely the electrostatic quadrupole voltage (V_Q), which determines the horizontal tune (ν_x), β function (β_x), and dispersion function (D_x), as well as the vertical tune (ν_y), β function (β_y), and dispersion function (D_y).

The injected beam enters the storage ring through a hole in the back-leg iron, and it emerges from the back-leg hole and enters into the superconducting inflector magnet [5, 20, 21]. During injection the muons are shielded from the dipole storage field by the inflector, where the double-cosine-theta design minimizes the flux leakage into the storage region. Although the inflector axis is tangent to the central orbit, the exit window is offset by 77 mm from the center of the storage region, resulting in orbits that would circle directly back to the inflector after one revolution. Three pairs of kicker plates [5, 22], positioned approximately 90° downstream of the inflector exit, create a sharp magnetic pulse (∼0.2 µs) that serves to kick the muon beam on the order of 10 mrad, centering it on the equilibrium orbit. The sub-optimal kick and mismatch between the inflector exit and storage region results in coherent beam motion, see Section VI A.

Two techniques are used to quickly remove muons living on the edge of the stored beam phase space distribution. First, the four quadrupole plates are ramped asymmetrically to full voltage. This process, known as scraping, leads to a systematic increase in the average vertical and radial position of the beam. As the beam shifts the muons at the edges of the beam distribution will scatter from one of the five copper collimators distributed around the ring, lose energy and spiral inward and out of the storage region. By the end of the scraping period the beam storage region is defined by the 90 mm diameter of the collimator aperture.

The positrons from the muon decays spiral inward and deposit their energy in the 24 calorimeters that are evenly spaced (every 15°) around the inside of the storage ring, where each calorimeter is made out of a 6×9 segmented array of lead(II) fluoride (PbF_2) crystals [5, 14, 15]. Straw tube tracker modules [5] installed in front of 2 calorimeter stations (located 180° and 270° from the injection point) detect the daughter electron trajectories, allowing for the reconstruction of the vertical and horizontal muon decay distributions. Muons injected on the central radius with precisely the magic momentum ($p_0 = 3.094\,\mathrm{GeV}/c$) and no transverse momentum will

Preliminary
DRAFT

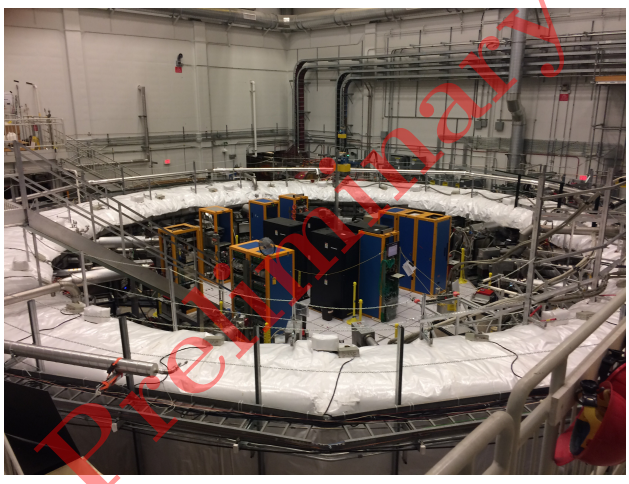

(a) Jason Picture of the storage ring. *Make a final decision on which picture to use.*

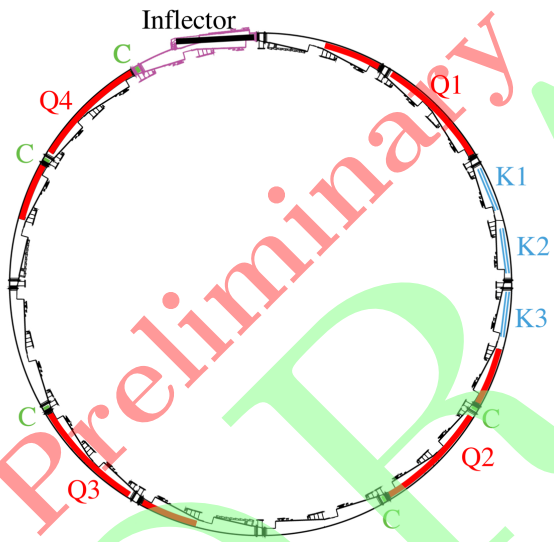

(b) David T. Diagram of the storage ring. *Finalize diagram with David T. and Leah.*

FIG. 3: The muon storage ring used by the Muon $g-2$ Experiment.

simply follow the circular design orbit. In reality, the beam has a momentum width of $\sim \delta p/p = 0.1\,\%$ and therefore a distribution of muon orbit radii. The muons with paths deviating from the magic radius are perturbed by the electric field gradient, inducing radial and vertical betatron oscillations that depend on the electric potential of the quadrupole plates.

Several detector packages were installed to measure beam injection parameters and oscillations in the storage

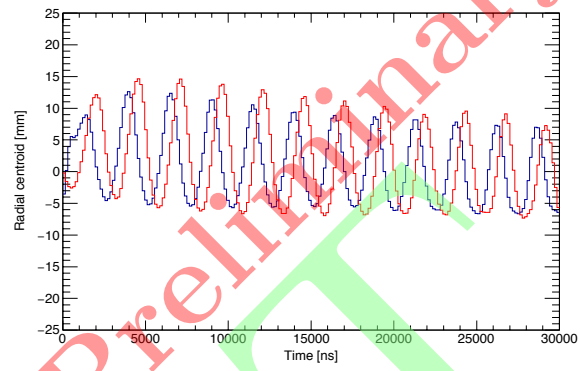

FIG. 4: Dat Horizontal position of centroid measured with the 180° fiber harp (blue) and 270° harp (red) for the first 30 µs of the fill. A discrete Fourier transform yields the horizontal tune. *Check with fiber harp experts.*

ring. As the muons exit the M5-line final focus upstream of the ring, they pass through two scintillator paddles used to register the time distribution of the incoming beam pulses. The relative intensities of the eight beam pulses are directly related to the integral of the pulse from T_0 detector [?]. The phase space of the injected beam is measured by the inflector beam monitoring system (IBMS) [?]. The IBMS is composed of three sets of scintillating fiber planes. The two sets placed upstream of the inflector are composed of a horizontal and a vertically strung plane, allowing for real time feedback while tuning the beam position and momentum. The third set has only a single vertically strung plane that is inserted downstream of the inflector and directly upstream of the first calorimeter after the inflector exit. The third IBMS detector is retracted during data-taking so that the wires and frame do not destructively interfere with the beam.

Two sets of retractable fiber harp beam monitors [3, 5] are located 180° and 270° downstream of the inflector exit. Each set has a horizontal and vertical plane constructed from seven parallel 0.5 mm diameter scintillating fibers with 13 mm spacing. The fiber harps directly measure the beam x-y beam motion after injection and through the period of kicker pulsing and quadrupole scraping. They are also used to measure the CBO oscillations of the beam centroid position and width at early times in the muon storage fill, see Figs. 4 and 5. Ultimately the fiber harps destructively interfere with the beam, and so they are retracted during production running. The beam characteristics are measured by the straw tracker detectors during production running, see Fig. 6.

Preliminary
Preliminary
DRAFT

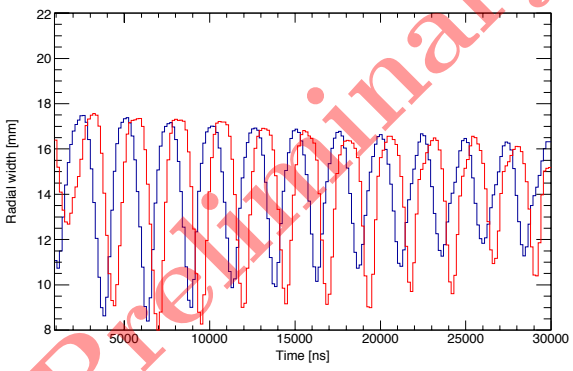

FIG. 5: Dat Horizontal width at 180° harp (blue) and 270° harp (red) over the first 30 µs of the fill. The deep modulation is a combination of β and D mismatch. *Check with fiber harp experts.*

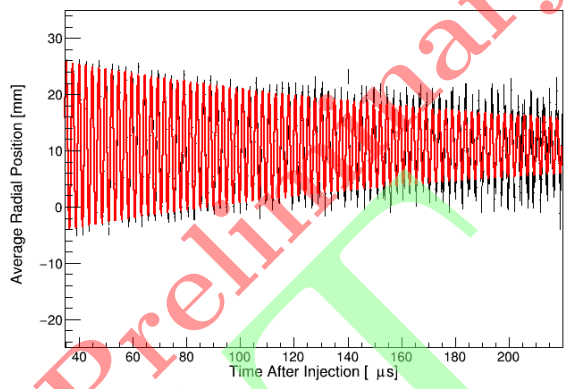

FIG. 6: David R. Radial centroid as measured with the 180° tracker over the first 220 µs of the fill. Red curve is a fitted damped sinusoid. Measurement is increasingly noisy at longer times as statistics are limited. *Check with tracker experts.*

IV. SIMULATION TOOLS

A. G4beamline

Diktys

The performance of the Muon Campus beamlines was simulated using G4beamline [23], a scripting tool for the GEANT4 Monte Carlo program. Using the GEANT4 [24] package, the code incorporates key particle-matter physical processes (e.g. energy loss, straggling, multiple scattering) as well as includes muon decays and precession of the muon spin. In the simulation, virtual detectors where placed at various locations along the beamline. As a result, it was possible to evaluate the population of secondaries, their 6D phase space distribution as well as the beam profiles over long distances. The code is also properly modified so that it fully incorporates all magnetic apertures according to the latest engineering specifications [10].

B. Phase Space Models

Mike

Analyses of particle distributions in phase space are performed for many expedient calculations and predictions pertaining to numerous run conditions. Matrices describing linear transverse particle motion are obtained based upon running conditions such as quadrupole high voltage setting, misalignments, and so on, and waveforms for the injection kicker can be superimposed upon the time distribution of an incoming beam pulse as well. Initial phase space distributions derived from Monte Carlo calculations of the beam production can be quickly analyzed by finding each particle's betatron oscillation amplitude about its ideal equilibrium orbit (horizontal and vertical) and determining immediately whether that particle can survive long term within the transverse aperture. With such information estimates of injection efficiencies, equilibrium momentum distributions, potential "lost muon" distributions and other phase space variable correlations can be quickly estimated and optimized for a variety of operational scenarios.

C. Bmad

David R.

BMAD refers to a subroutine library [25] for simulating the dynamics of relativistic beams of charged particles, and an associated format for defining beam line components. As long as the guide field components are defined according to BMAD conventions, the full complement of the analysis tools of the library can be used to investigate the particle dynamics, including various tracking methods, (Taylor maps, symplectic integration, Runge Kutta), construction of maps from tracking, evaluation of Twiss parameters, tracking through maps defined by maps or multipoles, etc. (For details see Bmad-Manual).

The BMAD formatted representation of the g-2 experiment is comprised of three distinct branches, 1)M5

Preliminary
Preliminary
DRAFT

beam line, 2)the injection channel through the back-leg iron and inflector, and the 3)storage ring including DC magnetic field, time dependent quadrupole electric fields and kicker magnetic fields, and collimator apertures. In the language of BMAD, 'branches' are joined at 'fork' elements and offsets with 'patches'.

The beam lines are assembled as a sequence of elements with fixed length. The electro-magnetic fields in each element are defined by field maps, multipole expansions, or analytic expressions. Time dependence for pulsed kickers and ramped quadrupoles requires custom code (as there is no appropriate standard BMAD module). Specialized custom routines can apply arbitrary kicker pulse shapes or quadrupole voltage time dependence.

Particle phase space and spin are tracked through the guide field using Runge-Kutta integration.

The program is equipped with a module to generate an initial distribution of muons, or to read a distribution from a file or both. For example, it is possible to generate a distribution gaussian in transverse phase space, with longitudinal distribution read from a file. (This is useful for imprinting the 'W' shaped longitudinal distribution on an otherwise gaussian transverse distribution.)

Lattice and phase space parameters are computed with standard BMAD routines, including Twiss parameters, beam moments, closed orbits, betatron tunes, chromaticity, synchrotron radiation, spin tunes, etc. The Jacobian matrices required to determine tunes and Twiss parameters are based on tracking.

Scattering is somewhat ad hoc. Muons entering the storage volume on trajectories that pass through quad plates, multiple scatter in the plates. Muons that are already inside the storage volume are lost if their trajectory subsequently intercepts a quad plate or collimator. If fiber monitors are active, muons multiply scatter in the fibers with energy loss consistent with measurements.

If the muon decay is turned on, then muons decay with lifetime assigned at birth. The phase space, spin coordinates and time of the decay at the decay point are recorded. A positron is created with momentum four-vector appropriately correlated with muon spin. The positron is tracked until it strikes a calorimeter plane, where phase space coordinates and time are recorded, or otherwise leaves the storage volume.

The walls of the inflector are defined as continuous apertures. Particles that hit the walls are lost. The ends of the inflector are treated as scattering planes.

1. *Quadrupoles*

The quadrupole plates are curved to preserve a fixed radial offset with respect to the central on momentum design orbit. The curvilinear coordinate system can be represented by beginning with a full 3-dimensional map, and then extracting an azimuthal slice of the map (in r, z at fixed ϕ) or with a fitted multipole expansion of McMillan functions. The curvature necessarily introduces nonlinearities that are not faithfully included in a 2 dimensional cartesian expansion. The BMAD code allows several possible ways to specify the quadrupole electric field.

1. Field map. The field map that is currently incorporated is based on a ρ, z azimuthal slice of of a 3 dimensional OPERA map. The quad map can be optionally defined as the sum of individual maps for each of the four plates, thus providing the flexibility to set the voltage independently on each plate, to model voltage errors, or the scraping configuration.

2. Multipole expansion. The multipole expansion in McMillan functions is derived as a fit to the azimuthal slice of the 3 dimensional map. An expansion in cartesian coordinates (that is inconsistent with Maxwell in the curved geometry) is another option. The multipole representations are convenient for exploring dependence on nonlinearity.

2. *Main Magnet*

The main magnet is represented as a map or analytic function with uniform field. A uniform radial component can be specified. Measured field errors are incorporated analytically. The azimuthal dependence of the error field is expanded as a solution to Laplace's equation in cylindrical coordinates in order to ensure consistency with Maxwell equations.

3. *Injection Channel*

The magnetic field through the hole in the back-leg iron and cryostat and main magnet fringe field is based on a 3 dimensional OPERA map. A distinct map is computed for the field in the inflector. The fringe and inflector maps are superimposed as appropriate.

The BMAD model has been used extensively to explore dependencies (capture efficiency, CBO amplitude, phase space distribution of captured beam, etc.) on injection trajectory, inflector orientation, field and aperture, kicker field amplitude, field profile, pulse shape, and timing, and quad voltage. Effects of quad field errors and misalignment on closed orbit and Twiss parameters have been studied. Simulations informed analysis of measurements with fiber harps. The flexibility to employ various quadrupole field profiles has enabled study of effects of nonlinearities on decoherence and debunching, electric field and pitch corrections. Indeed simulation will play a critical role in evaluation of the electric field and pitch systematics.

D. COSY INFINITY

Martin

DRAFT

E. gm2ringsim

Renee

In addition to modeling the electromagnetic fields and apertures of the beamlines and storage ring, it is at times illuminating to fully simulate material interaction effects, especially in the calorimeter, FBM and straw tracker systems. The reproduction in simulation of experimental observables, for example decay positron and lost muon signals in the calorimeters and track extrapolation in the straw trackers, allows for the estimation of systematic uncertainties due to interactions of the beam with storage ring components as well as analysis cuts and reconstruction techniques. These material effects, along with the static and time dependent electromagnetic fields and two types of beam guns are encapsulated into a GEANT4 [24] based package of the storage ring called gm2ringsim.

All ring components that could be traversed by the incoming muon beam have been replicated in gm2ringsim. Starting with the injection line, this includes the start time scintillators, the two IBMS detectors upstream of the inflector in the back-leg hole, the inflector coil and the last retractable IBMS detector installed immediately downstream of the inflector exit. CADMesh [26, 27] was used to accurately render the most complex solids, such as the vacuum chambers, IBMS detectors, trolly rails, quadrupole plates and the straw tracker modules. The CADMesh package ports CAD drawings into GEANT solids which can then be loaded during runtime. The remaining, simpler components, such as the kicker plates, calorimeter stations and fiber harps are constructed from native GEANT volumes. In order to reduce running time the simulation typically utilizes a parameterized shower response in the calorimeter PbF_2 blocks. The pole-tips, return yoke and service cryostats that surround the vacuum chambers are also included.

Multiple sets of time and space dependent magnetic fields are included in the gm2ringsim package. The static fields, such as the inflector and magnetic dipole fringe fields are mapped using OPERA *[get citation]* simulations. The magnetic field in the storage region is modeled as pure dipole with the option of turning on precision maps of magnetic multipole and radial fields as measured by the field team. The time dependence of the magnetic pulse delivered by the kicker plates is extracted from oscilloscope traces *[do we want to include a figure of a trace here? Or should we refer to the kicker paper?]* and is scaled according to the measured peak delivered magnetic kick. The electric quadrupole fields are implemented with analytical calculations that include measured multipole values in the storage regions, while a map is used for the region between the outside of the quadrupole plates and the inside wall of the vacuum chambers. This field is particularly important for the set of quadrupole plates positioned after the inflector, as a the injected beam is off orbit and traverses the region between the plate and the vacuum chamber.

The gm2ringsim package includes several types of particle guns, the most commonly used are the beam gun and the gas gun. The beam gun is designed to replicate the experimental injection process and is most often utilized to study the motion of injected muons inside the ring. The beam gun allows the user to tune the phase space parameters of the injected beam and provides the option of using as input the distribution of muons at the exit of the M4/M5 line, as determined from g4beamline simulations. The beam gun also has the capability to shoot multiple particles per event and include other particles species, for example protons and positrons, in the beam distributions. Beam gun simulations are computationally expensive, requiring stored muons to be tracked as they circulate for up to 700 µs around the storage ring. For studies requiring only information about the muon decay point and subsequent positron motion it is more efficient to use the gas gun. The gas gun simulates the spatial distribution, including distortions due to coherent betatron oscillations, of the decay positions of the stored muons in the beam. The positrons born at these decays positions are then tracked through the ring as they spiral inwards, creating signals in the calorimeters and tracker detectors.

V. STORAGE RING OPTICS

Martin

We need to define the basic beam dynamics quantities of interest! This section seems like a reasonable place to do it. It would also be nice to have some clear definition and or derivation of the field index (n). In the linear model of small betatron oscillations (simple harmonic motion) with dipole and quadrupole fields, one has

$$\delta(s) \equiv \frac{p - p_0}{p_0}. \tag{7}$$

$$\eta_x(s) \equiv \frac{dx}{d\delta} \approx \frac{R_0}{1-n}. \tag{8}$$

$$x_e(s) = \eta_x(s)\,\delta(s). \tag{9}$$

$$\begin{aligned} x(s) &= x_e(s) + \sqrt{\epsilon_x \beta_x(s)}\cos\left[\nu_x \phi(s) + \phi_x^0(s)\right], \\ x'(s) &\equiv \frac{dx}{ds}. \end{aligned} \tag{10}$$

$$\begin{aligned} y(s) &= \sqrt{\epsilon_y \beta_y(s)}\cos\left[\nu_y \phi(s) + \phi_y^0(s)\right], \\ y'(s) &\equiv \frac{dy}{ds}. \end{aligned} \tag{11}$$

Figure 7 shows horizontal and vertical tunes along the voltage contour. The β and η functions for quad voltage of 20.4 kV are shown in Fig. 8. *Someone should say*

DRAFT

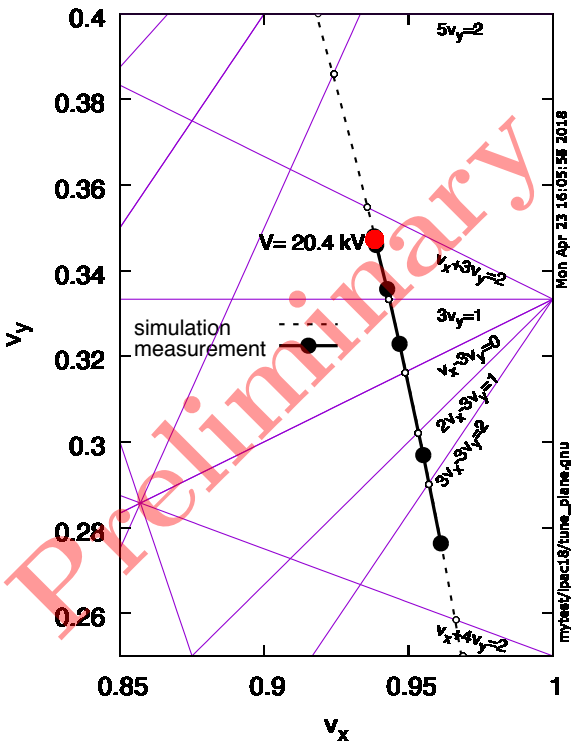

FIG. 7: David R. Dependence of tune on quadrupole voltage computed with a Bmad based model of the guide field. Resonance lines are shown. Typical operating point is 20.4 kV (red dot). *Change red point to 18.3 kV; update black points with Run-2 fiber harp data; remove timestamp and directory info.*

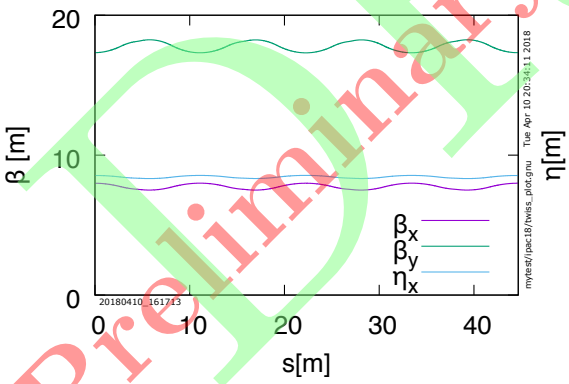

FIG. 8: David R. and David T. Twiss parameters in the closed storage ring. *Harmonize notation; remove timestamp and directory info.*

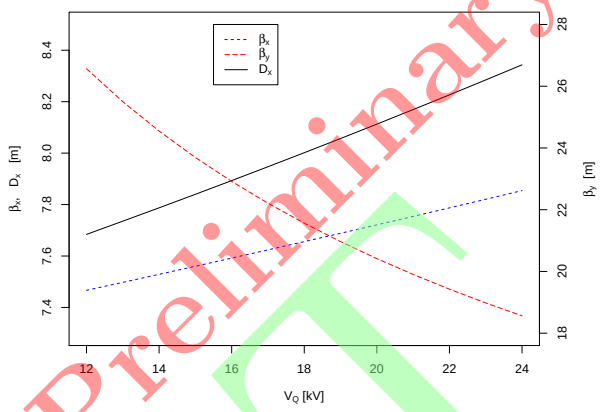

FIG. 9: Mike and David T. Dependence of horizontal and vertical amplitude functions and horizontal dispersion function on the electrostatic quadrupole system high voltage. The values are for one point in the ring, namely at the entrance to the ring at the end of the inflector.

something about the dependence of Twiss parameters on V_{quad}, see Fig. 9.

The dependencies of the optical functions of the ring on the quadrupole system high voltage are shown in Figure 9.

The quadrupole field is superimposed on the main dipole field. The reference trajectory through the quadrupoles has significant curvature and the quadrupoles share that curvature. As a result, the quadrupole field is necessarily nonlinear, with a significant sextupole term. An effect of this and other nonlinearities associated with the geometry of the quad electrodes is an amplitude dependence of the tunes. The tune shifts associated with the various quad multipoles [18] are shown in Fig. 10. Figure 11 shows that the magnetic field imperfections also lead to amplitude-dependent tune shifts. The magnetic field *Someone should say something about the tune dependence on momentum and chromaticity dependence on quadrupole voltage, see Figs. 12 and 13.* The nonlinearities of the electrostatic quadrupoles, as well as residual magnetic multipoles [5] can drive resonances (see Fig. 7). Operation near resonances is avoided to mitigate losses. A tune scan that extends over the operating region is shown in Fig. 14. The storage fraction is measured as quadrupole voltage is increased from 18 kV to 23 kV. The degraded storage fractions evident at 18.8 kV and 21.2 kV correspond to the $3\nu_x = 1$ and $\nu_x + 3\nu_y = 2$ resonances.

Figure 12 indicates the horizontal and vertical betatron tune shifts from nominal values due to deviations

Preliminary
DRAFT
Preliminary
Preliminary

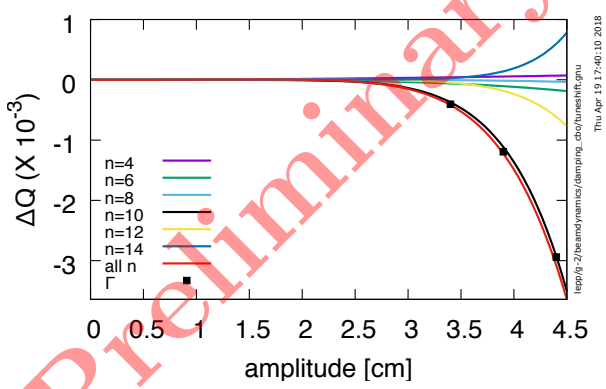

FIG. 10: David R. Simulated contribution to amplitude dependent tune shift from each of the quad multipoles, their sum, and the decoherence rate Γ as determined by tracking. *Harmonize notation; remove timestamp and directory info.*

in momentum from the central value. For this figure the central tunes would be $\nu_x = 0.945$ and $\nu_y = 0.329$ for a nominal quadrupole high voltage of 18.3 kV.

The guide field is characterized by measurements of closed orbit, tunes, and modulation of the beam width and centroid. Measurements of the tunes with the fiber harps are shown in Fig. 7. *Someone should say something about the tune footprint, see Fig. 15.*

A. Injection

David R.

Maybe we should put IBMS and T0 figures in this section, as they provide beam information just before injection.

The beam is injected into the ring through a hole in the back leg iron. The 1.7 m long superconducting inflector bucks the main dipole field so that the beam traverses the inflector without significant deflection and exits the inflector on a trajectory tangent to a displaced circular orbit. The beam crosses the design orbit in the gap of the pulsed kicker that steers the beam radially outward and onto the central orbit as shown in Fig. 3.

The inflector aperture (18 mm horizontally by 56 mm vertically) is very much smaller than the aperture of the ring (90 mm round). In order to maximize transmission, the beam is focused to a narrow waist through the inflector and with zero dispersion.

Manipulation of the beam width to maximize transmission through the inflector and into the ring is illustrated in Fig. 16. The mismatch of β and η functions leads to a modulation of beam width with components at the betatron frequency and twice the betatron frequency respectively. The relative contribution of betatron motion and momentum offset to the width can be extracted from the width measurement (Fig. 5) by suitable decomposition. The phase space at the inflector exit is defined by the inflector aperture and shown in Fig. 17.

The kicker is located $\phi_\beta = \pi/2$ downstream from the injection point at the inflector exit. The beam crosses the design orbit with an angle determined by the radial displacement of the inflector axis (nominally 77 mm from the design orbit and indicated as 'd' in Fig. 3), and the exit angle. The crossing angle, and therefore the kick required to steer the beam onto the closed orbit, is minimum if the exit angle is zero. The dependencies can be made quantitative with a few simplifying assumptions, namely that the β and η functions are uniform around the ring, and as long as we treat the kickers as a δ-function in azimuthal angle. (The kickers [5, 22] in fact extend over about 36° of arc). With these assumptions, the horizontal displacement of the trajectory is

$$\begin{aligned} x(s) &= (x_{\text{inf}} - \delta\eta)\cos[\phi(s)] + \eta\delta \\ &\quad - k\beta_0 \cos[\phi(s)] + x'_{\text{inf}} \sin[\phi(s)] \\ &= A\cos[\phi(s) + \phi_0] + \eta\delta, \end{aligned}$$

where $x_{\text{inf}}, x'_{\text{inf}}$ are the displacement and angle of the trajectory at the inflector exit, η the dispersion, δ is the fractional momentum offset, k is the kick angle, $\phi(s)$ the betatron phase advance with $s = 0$ at the injection point,

$$\begin{aligned} A &= \pm\sqrt{(x_{\text{inf}} + \delta\eta - k\beta)^2 + (x'_{\text{inf}}\beta)^2} \\ \tan\phi_0 &= \frac{x'_{\text{inf}}\beta}{x_{\text{inf}} - \delta\eta - k\beta}. \end{aligned}$$

The extremes of the displacement of the motion, that is the envelope of the motion is given by $x_{\text{ext}} = \pm|A| + \eta\delta$. The envelope is plotted in Fig. 18 as a function of momentum for three different injection angles, and for a kick angle $k = 8$ mrad, which is about 80 % of the nominal kick. The minimum momentum that can be stored decreases as the kicker angle approaches nominal. Under kicking skews the momentum distribution high. Kick and and injection angle both contribute to the amplitude of the oscillations about the closed orbit. Non zero injection angle reduces momentum acceptance symmetrically about zero.

Figure 19 needs to be discussed somewhere in the text.

B. Average Tune & Chromaticity Measurements

Dat

The horizontal (ν_x) and vertical (ν_y) tunes are defined

Preliminary
DRAFT

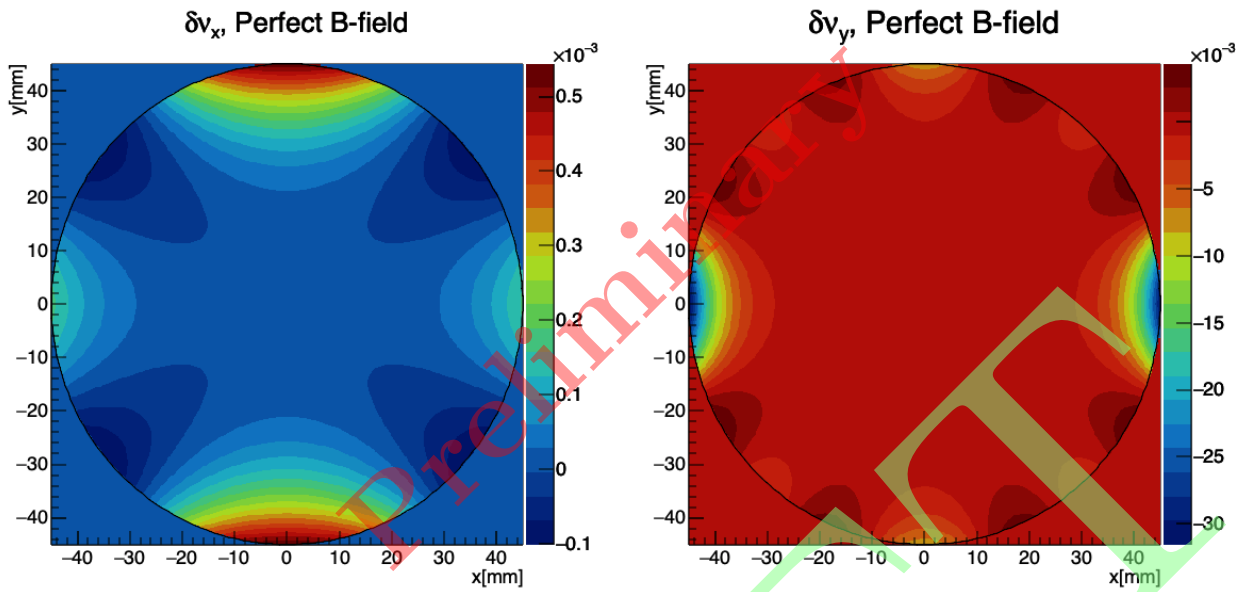

FIG. 11: David T. Amplitude-dependent tune shifts ($\delta = p_x/p_0 = p_y/p_0 = 0$) within the storage region ($r \leq 45\,\mathrm{mm}$) for an ideal magnetic field. *Harmonize notation.*

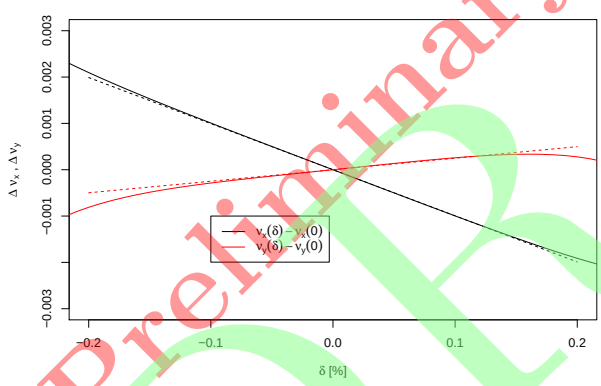

FIG. 12: Mike and David T. Dependence of zero-amplitude horizontal and vertical betatron tunes from their design values as functions of relative momentum deviation, for a quadrupole system high voltage of 18.3 kV. *Define the dashed lines.*

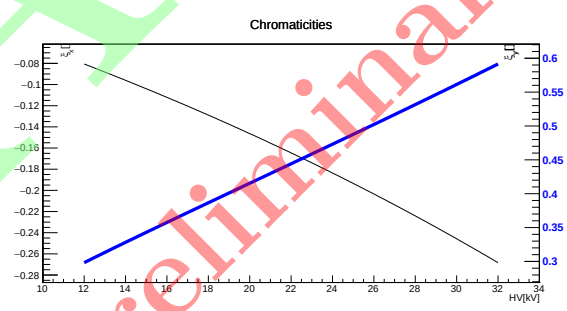

FIG. 13: David T. Chromaticity dependence on quadrupole voltage. *Harmonize notation; is this chromaticity or relative chromaticity; needs legend; readable font size.*

as

$$\nu_x \equiv \mathcal{N}_x = \frac{\mathcal{N}_x/\mathcal{T}}{1/\mathcal{T}} = \frac{f_x}{f_c} = 1 - \frac{f_{\mathrm{cbo}}}{f_c}$$
$$\nu_y \equiv \mathcal{N}_y = \frac{\mathcal{N}_y/\mathcal{T}}{1/\mathcal{T}} = \frac{f_y}{f_c} = \frac{1}{2}\left(1 - \frac{f_{\mathrm{vw}}}{f_c}\right), \qquad (12)$$

where $\mathcal{N}_x$ is the number of horizontal betatron oscillations per 1 turn around the storage ring, $\mathcal{T}$ is the time it takes traverse 1 turn around the storage ring, f_x is the horizontal betatron frequency, f_c is the cyclotron frequency, f_{cbo} is the coherent betatron oscillation frequency, $\mathcal{N}_y$ is the number of vertical betatron oscillations per 1 turn around the storage ring, f_y is the vertical be-

DRAFT Preliminary Preliminary Preliminary

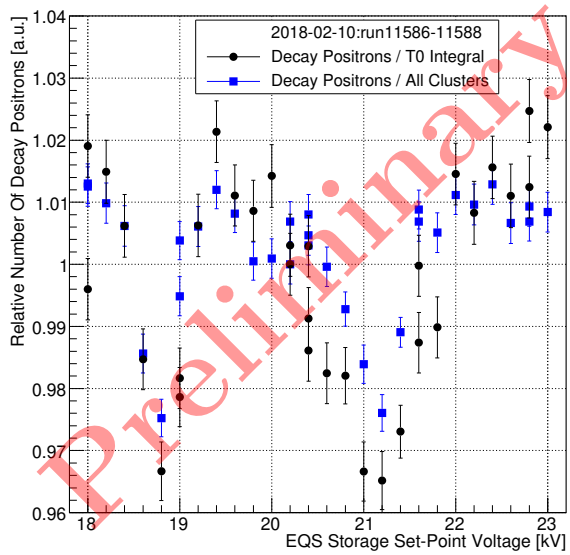

(a)

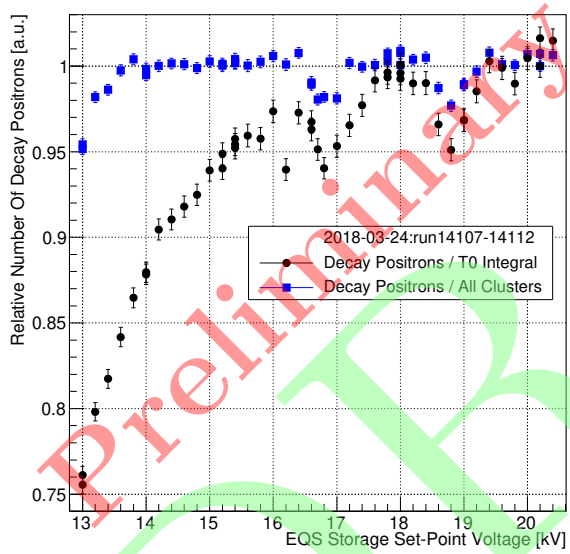

(b)

FIG. 14: Sudeshna Relative number of decay positrons in a fill as a function of quadrupole voltage. Storage efficiency is degraded by betatron resonances at 18.8 and 21.2 kV. *Harmonize notation; update with Run-2 calo data; do we need to compare to Run-1 data.*

tatron frequency, and f_{vw} is the vertical waist frequency.

Figure 20 needs to be discussed somewhere in the text.

The electrostatic quadrupole system produces vertically focusing and horizontally defocusing, where the V_Q settings need to be translated into beam dynamics parameters to help understand the operational behavior

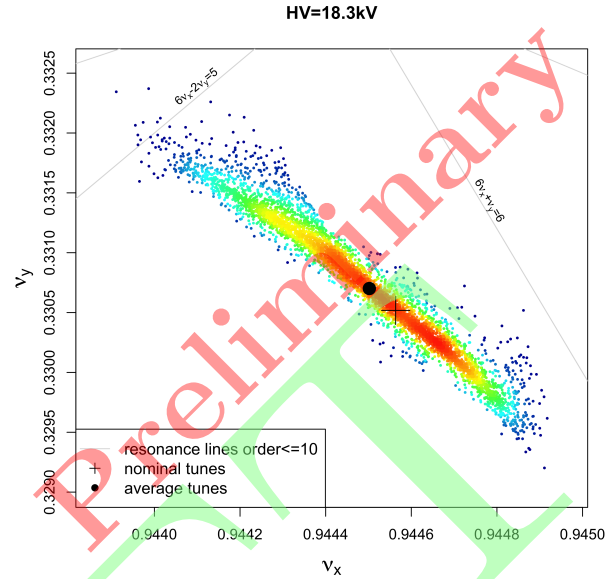

FIG. 15: David T. Tune footprint of a beam distribution at 149 µs after injection and for a magnetic field measurement. *Remake with the ideal magnetic field; add a z-axis that defines the color range.*

of the storage ring. The FBM, trackers, and calorimeters can be used to measure the average cyclotron ($\langle f_c \rangle$), coherent betatron oscillation ($\langle f_{\mathrm{cbo}} \rangle$), vertical betatron ($\langle f_y \rangle$), and vertical waist ($\langle f_{\mathrm{vw}} \rangle$) frequencies. These average frequencies can in turn be used to determine the average horizontal ($\langle \nu_x \rangle$) and vertical ($\langle \nu_y \rangle$) tunes, see Table II.

For a circular storage ring with a perfect dipole magnetic field (B_0), the field index inside of a quadrupole (n_0) is defined as

$$n_0 \equiv \frac{m\gamma r}{pB_0}\frac{\partial E_r}{\partial r}, \tag{13}$$

where m is mass, γ is the Lorentz factor, r is the radial distance from the center of the storage ring, p is momentum, and E_r is the radial component of the quadrupole electric field.

Figure 21 needs to be discussed somewhere in the text.

The smoothed quadrupole model describes the EQS as being continuous around the entire storage ring. The effective field index (n) in the smoothed model is defined as

$$n \equiv \left(\frac{4l_q}{C_0}\right) n_0 = \left(\frac{l_q/R_0}{\pi/2}\right) n_0, \tag{14}$$

where $R_0 = 7112\,\mathrm{mm}$ is the storage ring equilibrium orbit radius, $C_0 = 2\pi R_0$ is the storage ring equilibrium orbit circumference, and l_q is the quadrupole long-short pair length.

Preliminary
Preliminary
Preliminary
DRAFT

TABLE II: Dat Measured $\langle f_c \rangle$, $\langle f_{\rm cbo} \rangle$, and $\langle f_y \rangle$ (only statistical errors are given) along with the corresponding $\langle \nu_x \rangle$ and $\langle \nu_y \rangle$ calculated via Eq. (12). This data was collected during Run-1 with the 180° horizontal and vertical fiber harp central (no. 4) fibers, where the first 3 µs of data are not used for these measurements. The $\langle f_c^x \rangle$ is the $\langle f_c \rangle$ measured by the horizontal fiber harp and used to calculate $\langle \nu_x \rangle$, while the $\langle f_c^y \rangle$ is the $\langle f_c \rangle$ measured by the vertical fiber harp and used to calculate $\langle \nu_y \rangle$. *Update with Run-2 fiber harp data; do we need to compare to Run-1 data.*

$V_{\rm Q}$ [kV]	$\langle f_c^x \rangle$ [MHz]	$\langle f_{\rm cbo} \rangle$ [MHz]	$\langle \nu_x \rangle$	$\langle f_c^y \rangle$ [MHz]	$\langle f_y \rangle$ [MHz]	$\langle \nu_y \rangle$
13.0	6.697(5)	0.2600(30)	0.9612(4)	6.715(5)	1.8555(50)	0.2763(8)
15.0	6.697(5)	0.3005(30)	0.9551(4)	6.715(5)	1.9940(50)	0.2969(8)
17.6	6.697(5)	0.3553(30)	0.9469(4)	6.715(5)	2.1680(50)	0.3229(8)
19.0	6.697(5)	0.3845(30)	0.9426(5)	6.715(5)	2.2540(50)	0.3357(8)
20.2	6.697(5)	0.4100(30)	0.9388(5)	6.715(5)	2.3235(50)	0.3460(8)
20.5	6.697(5)	0.4143(30)	0.9381(5)	6.715(5)	2.3370(50)	0.3480(8)

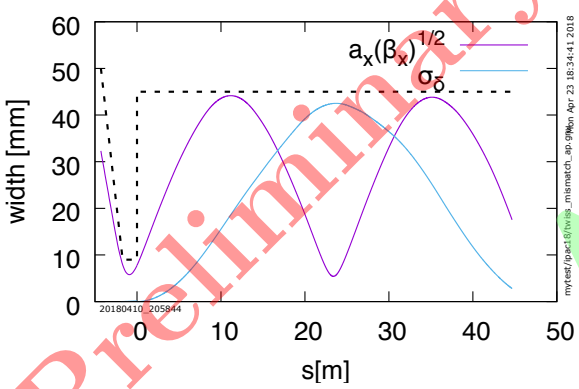

FIG. 16: David R. Propagating beam betatron and energy width through narrow aperture inflector and into the storage ring. The dashed line is the horizontal aperture. *What are $a_x\left(\beta_x\right)^{1/2}$ and σ_δ; is the y-axis label really right; remove timestamp and directory info.*

The smoothed model approximates [18] the storage ring tunes as

$$\begin{aligned} \nu_x &\approx \sqrt{1-n} \\ \nu_y &\approx \sqrt{n}. \end{aligned} \tag{15}$$

Figure 22 needs to be discussed somewhere in the text.

The discrete quadrupole model describes the EQS as being a set of 4 separate quadrupoles that have a four-fold symmetry around the storage ring. The discrete model approximates [18] the storage ring tunes as

$$\begin{aligned} \cos\left(\frac{\pi}{2}\nu_x\right) &\approx c_i \cos\left(\frac{l_q}{R_0}\sqrt{m}\right) \\ &\quad - \frac{1}{2} s_i \left(\sqrt{m} + \frac{1}{\sqrt{m}}\right) \sin\left(\frac{l_q}{R_0}\sqrt{m}\right) \\ \cos\left(\frac{\pi}{2}\nu_y\right) &\approx \cos\left(\frac{l_q}{R_0}\sqrt{n_0}\right) \\ &\quad - \frac{1}{2}\frac{l_i}{R_0}\sqrt{n_0} \sin\left(\frac{l_q}{R_0}\sqrt{n_0}\right), \end{aligned} \tag{16}$$

where $c_i \equiv \cos\left(l_i/R_0\right)$, $s_i \equiv \sin\left(l_i/R_0\right)$, $m \equiv 1 - n_0$ and l_i is the interval length between quadrupole long-short pairs. The following numerical relations obtained from [18] are assumed for Eq. (16): $l_i/R_0 = 0.895354$, $l_q/R_0 = 0.675442$, and $n_0 = n/0.43$.

Equations (13) and (14) show that $n \propto \partial E_r/\partial r$, and $E_r \propto V_{\rm quad}$ when assuming that the quadrupole geometry and HV pulse generation are independent of $V_{\rm quad}$, which then implies that $n \propto V_{\rm quad}$:

$$n = \sigma V_{\rm quad}, \tag{17}$$

where σ is the proportionality constant (conversion factor) between n and $V_{\rm quad}$ *[need to pick a different symbol for σ, as it gets confusing when talking about the standard deviation difference]*. Equation (17) is combined with Eqs. (15) and (16), and the resulting functions are fit to the $\langle \nu_x \rangle$ and $\langle \nu_y \rangle$ data in Table II, see Fig 23. The σ_x^s, σ_y^s, σ_x^d, and σ_y^d fit parameters in Fig. 23 correspond to the σ in Eq. (17). In the ideal case, $\sigma_x^s = \sigma_y^s$ and $\sigma_x^d = \sigma_y^d$.

The $\chi^2/{\rm ndf} < 1$ for all of the fits in Fig. 23, which indicates that the precision of the fit parameters is limited by the "large" size of the data point errors. There is some mild tension between the horizontal and vertical tune fits within each model, as

$$\begin{aligned} \frac{\left|\sigma_x^s - \sigma_y^s\right|}{\sqrt{\left(\delta_x^s\right)^2 + \left(\delta_y^s\right)^2}} &= 1.990\,\sigma \\ \frac{\left|\sigma_x^d - \sigma_y^d\right|}{\sqrt{\left(\delta_x^d\right)^2 + \left(\delta_y^d\right)^2}} &= 2.147\,\sigma, \end{aligned} \tag{18}$$

Preliminary
DRAFT

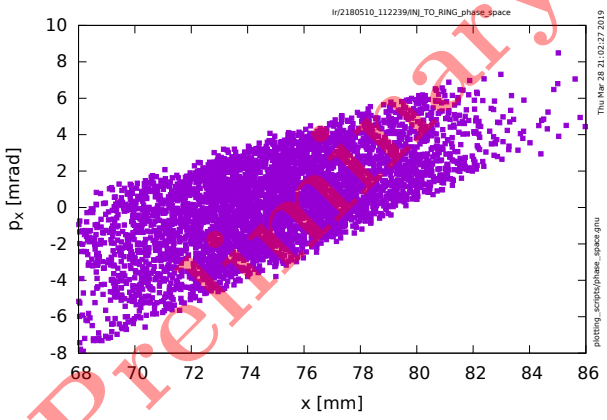

(a) Horizontal phase space at the exit of the inflector.

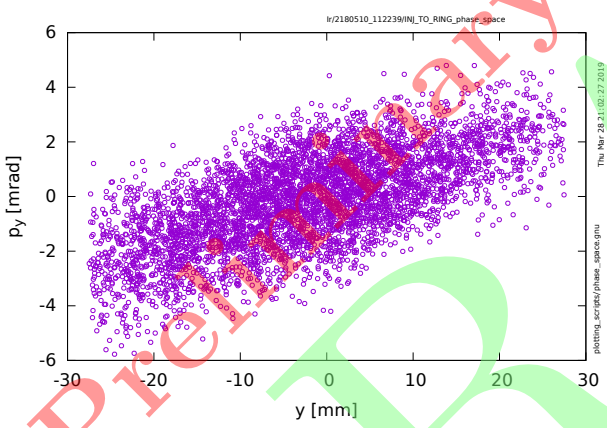

(b) Vertical phase space at the exit of the inflector.

FIG. 17: David R. Simulated muon beam phase space at the downstream end of the inflector. *Harmonize notation; show full coordinate ranges; change from scatter plot to 2D histogram; remove timestamp and directory info.*

where δ_x^s, δ_y^s, δ_x^d, and δ_y^d are the errors for the σ_x^s, σ_y^s, σ_x^d, and σ_y^d values respectively. This tension is likely due to some undetermined systematic effect in the tune data. This tension can be eliminated by rescaling the errors so that the standard deviations difference is $1\,\sigma$, where these multiplicative scale factors are $\epsilon^s = 1.990$ and $\epsilon^d = 2.147$ for the smoothed and discrete models respectively.

The horizontal and vertical fit parameters can be av-

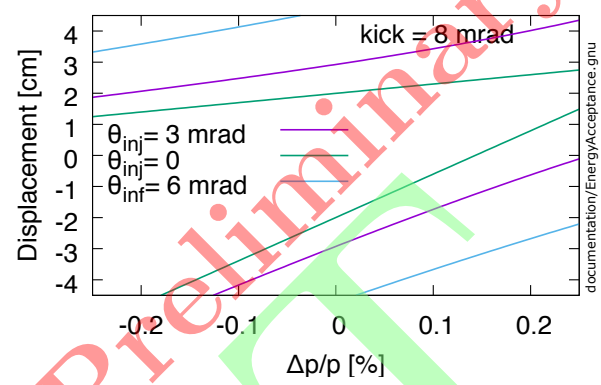

FIG. 18: David R. Kick angle ∼80 % of nominal. The green lines mark the envelope of the motion of a muon that exits the inflector with zero angle. The on momentum muon oscillates between ±2 cm. If momentum offset is 0.2 % the peak to peak oscillation is ∼5 mm. A muon with momentum offset of −0.18 % is outside the 4.5 cm aperture. *Harmonize notation; should we change 80 % nominal kick to 90 % nominal kick as* 149 kV/165 kV = 0.9*; remove timestamp and directory info.*

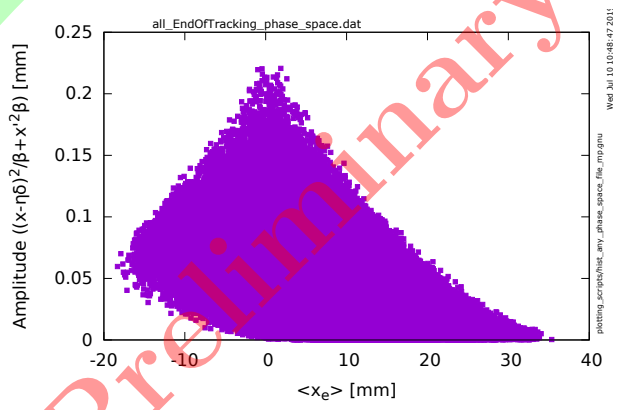

FIG. 19: David R. Horizontal betatron amplitude vs. average equilibrium position for stored muons. *Harmonize notation; check units used for calculations; change scatter plot to 2D histogram; remove timestamp and directory info.*

Preliminary
DRAFT

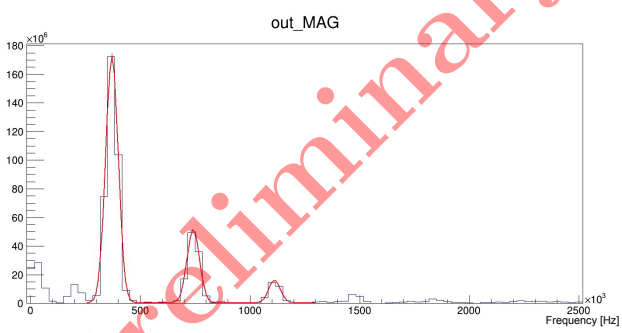

(a)

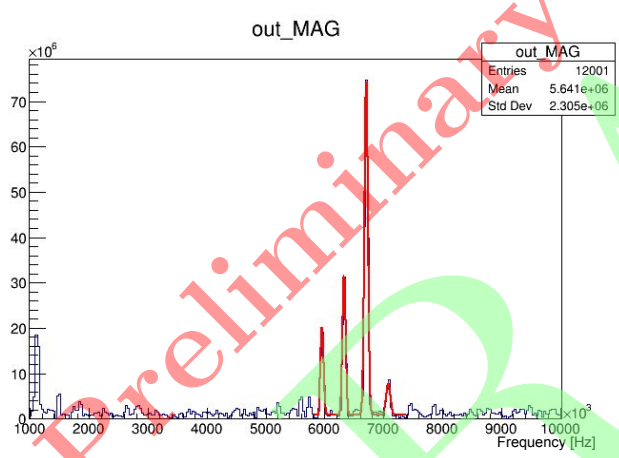

(b)

FIG. 20: Dat A sum of Gaussian functions is fitted to the FFT of the fiber harp signals to extract the $\langle f_{\mathrm{cbo}}\rangle$, $\langle f_y\rangle$, $\langle f_{\mathrm{vw}}\rangle$, $\langle f_x\rangle$, and $\langle f_c\rangle$ values for a given V_Q setting. *What do we really want to show?*

eraged to produce a final estimation of the conversion factor between n and V_{quad}:

$$\begin{aligned}\sigma^s &= \frac{1}{2}\left(\sigma_x^s + \sigma_y^s\right) \pm \frac{1}{2}\sqrt{\left(\epsilon^s\delta_x^s\right)^2 + \left(\epsilon^s\delta_y^s\right)^2} \\ &= (5.886 \pm 0.023)\times 10^{-3}\,\mathrm{kV}^{-1} \\ \sigma^d &= \frac{1}{2}\left(\sigma_x^d + \sigma_y^d\right) \pm \frac{1}{2}\sqrt{\left(\epsilon^d\delta_x^d\right)^2 + \left(\epsilon^d\delta_y^d\right)^2} \\ &= (5.892 \pm 0.025)\times 10^{-3}\,\mathrm{kV}^{-1}, \end{aligned} \tag{19}$$

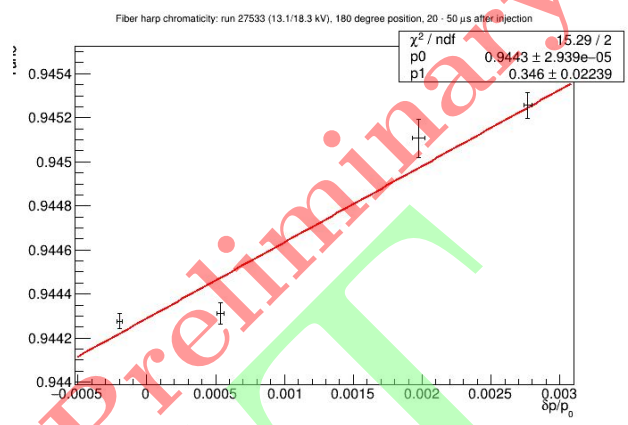

FIG. 21: Dat A measurement of $\langle\nu_x\rangle$ versus $\langle\delta\rangle$ for $V_Q = 18.3\,\mathrm{kV}$, where the slope of the fit line gives an estimate of $d\nu_x/d\delta$. This data was collected during Run-2 with the 180° horizontal fiber harp. *What do we really want to show?*

TABLE III: Dat Field index and tune values based on the smoothed model for different quadrupole storage voltages used in Run-1 data collection, see Eqs. (15), (17), and (19), along with the numerical relation $n_0 = n/0.43$ obtained from [18]. *Should the field indices also be calculated using the discrete model?*

V_{quad} [kV]	n_0	n	ν_x	ν_y
15.0	0.20533(80)	0.08829(35)	0.95484(18)	0.29714(58)
18.3	0.25050(98)	0.10771(42)	0.94461(22)	0.32820(64)
20.4	0.2792(11)	0.12007(47)	0.93804(25)	0.34652(68)

where σ^s and σ^d are the average conversion factors for the smoothed and discrete models. Equations (18) and (19) show that the smoothed and discrete models produce consistent results, and Table III provides Run-1 field index and tune values that are based on the smoothed model *[maybe this should also be done for the discrete model]*.

C. Closed Orbit & Quadrupole Distortions

Mike

Distortions of the closed orbit and of the amplitude functions are created due to misalignments of the electrostatic quadrupole plates and imperfections of the magnetic field. Systematic displacement of a pair of quadrupole plates (horizontal or vertical) will create horizontal or vertical orbit distortions. Likewise, local devia-

Preliminary
Preliminary
Preliminary
DRAFT

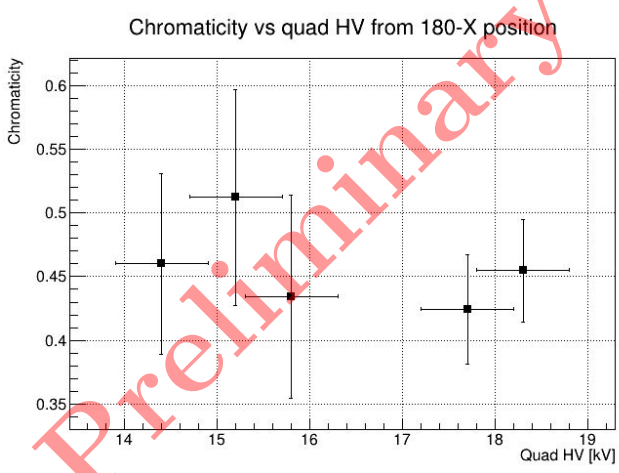

FIG. 22: Dat An estimate of $d\nu_x/d\delta$ versus V_Q that is based on fiber harp data. This data was collected during Run-2 with the 180° horizontal fiber harp. *What do we really want to show?*

tions in the vertical or radial magnetic field components will cause deviations in the horizontal or vertical components of the closed orbit, respectively. Assembly of the electrostatic quadrupole included measurement and fiducialization of the plate locations and, upon installation and alignment, provide knowledge of final placement. Table IV shows the average measured residual displacements of plate pairs for the eight electrostatic quadrupoles in the Storage Ring. Non-zero values of dx and dy will steer the beam horizontally or vertically, while dax and day – deviations in plate separation – alter the focusing strength of the quadrupoles and hence introduce beam envelope distortions. In addition, from Fig 2, closed orbit and focusing distortions can be ascertained from the dipole and quadrupole errors of the main magnetic field.

Figures 24 and 25 show the effects computed from the errors described above. We see that expected orbit distortions will be on the scale of 2 mm in both the horizontal and vertical planes, and that amplitude function distortions will be on the scale of a few percent, mostly due to a strong, local quadrupole magnetic field error near the entrance to the Storage Ring due to the inflector magnet.

VI. SYSTEMATICS

Bill: People want to know how this affects the physics. The quad non-linearities (mainly 20-pole) make the CBO de-cohere faster. Jason has shown that this gives a smaller CBO systematic error. I don't think the 20-pole

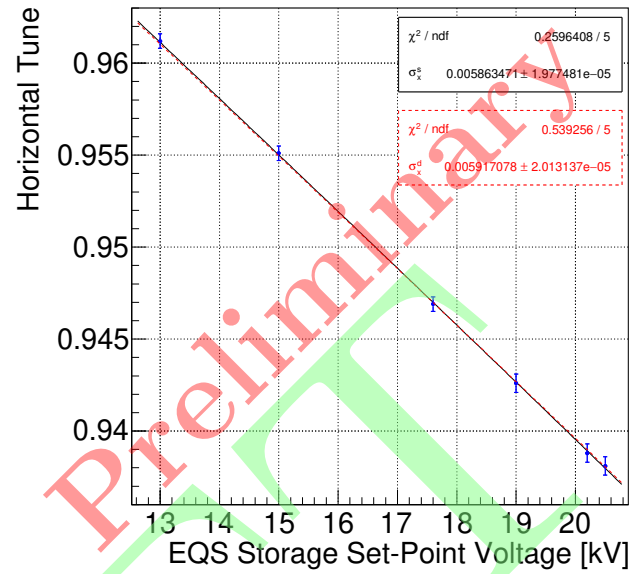

(a) $\langle\nu_x\rangle$ vs. V_{quad}

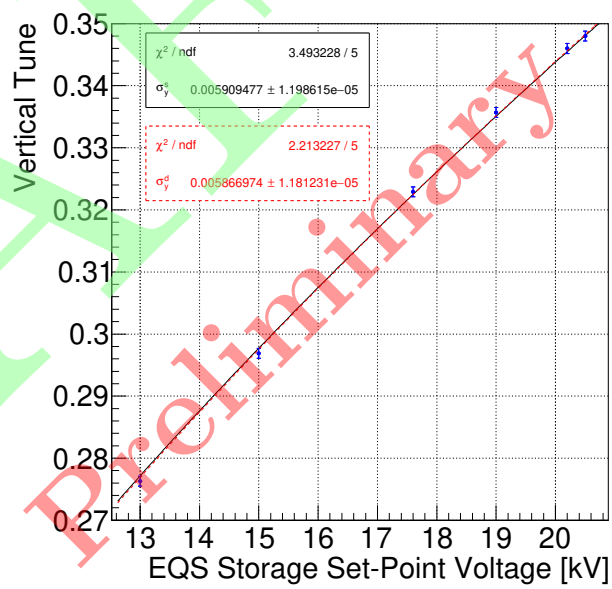

(b) $\langle\nu_y\rangle$ vs. V_{quad}

FIG. 23: Dat Average tune data (blue circular points), see Table II, along with fits using the smoothed quadrupole model (solid black lines) and discrete quadrupole model (red dashed lines), see Eqs. (15), (16), and (17). The σ_x^s, σ_y^s, σ_x^d, and σ_y^d fit parameters are for the smoothed model fit to $\langle\nu_x\rangle$ data, smoothed model fit to $\langle\nu_y\rangle$ data, discrete model fit to $\langle\nu_x\rangle$ data, and discrete model fit to $\langle\nu_y\rangle$ data respectively. *Harmonize notation; update with Run-2 fiber harp data; do we need to compare to Run-1 data; should we add gm2ringsim tune curves.*

DRAFT

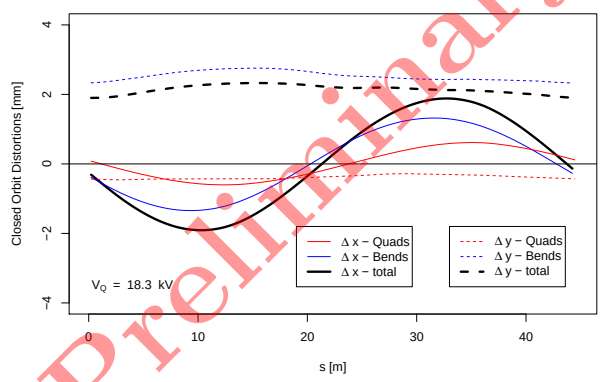

FIG. 24: Mike and David T. Computed horizontal (solid) and vertical (dashed) closed orbit distortions due to quadrupole plate alignment errors (red) and main dipole field errors (blue); the heavy black curves are the sum of the effects from the quadrupole and dipole errors. *Check with field, tracker, & quad experts.*

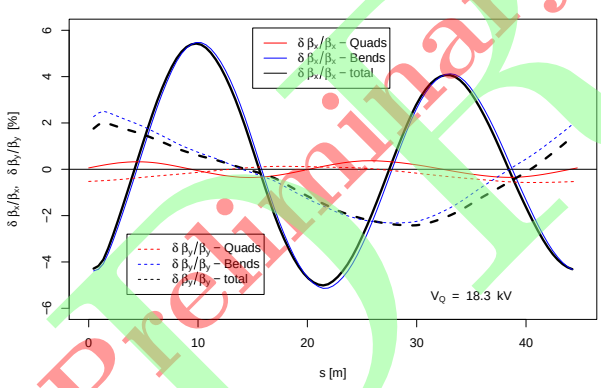

FIG. 25: Mike and David T. Computed horizontal (solid) and vertical (dashed) amplitude function distortions due to quadrupole plate alignment errors (red) and main dipole field gradient errors (blue); the heavy black curves are the sum of the effects from the quadrupole and dipole errors. *Harmonize notation; check with field, tracker, & quad experts.*

TABLE IV: Mike Quadrupole in situ alignment data; dx and dy indicate the displacement of the center of quadrupole plate pairs which will generate steering, while dax and day are the deviations in plate pair separation which will affect the focusing strength of the quadrupoles.

Quadrupole	dx [mm]	dy [mm]	dax [mm]	day [mm]
Q1S	-0.325	2.235	0.265	0.185
Q1L	-0.245	-0.980	0.285	-0.140
Q2S	-0.995	-0.675	-0.295	-0.185
Q2L	-0.035	0.380	-0.095	-0.290
Q3S	-0.20	0.75	0.20	-0.41
Q3L	0.115	-1.965	-0.195	-0.125
Q4S	2.045	-1.315	0.195	-0.155
Q4L	0.085	-0.220	-0.115	0.220

affects the E-field correction too much. Those are the two physics issues I can think of for the 20-pole quad non-linearity. Also, there are 20-pole betatron resonances which give higher lost muon rates (see David Tarazona's docdbs), but we avoid them.

A. Coherent Beam Motion & Detector Acceptance

Jason

The muon beam exhibits coherent motion inside of the storage ring due to several effects. The non-ideal magnetic kicker pulses produce a horizontal (radial) modulation of the beam centroid with characteristic frequency f_x, as the centroid is not kicked onto the the central orbit (magic) radius. Injection angle errors produce a vertical modulation of the beam centroid with characteristic frequency f_y, but these errors and corresponding vertical modulation are very small. There is a mismatch between the 18 mm (width) × 56 mm (height) Inflector aperture [20, 21] and circular cross section of the storage region, which has a 90 mm diameter. The Inflector aperture imposes a minimum beam spot (waist) at injection, and so there is a modulation of the beam width as the collection of particles rotates in phase space.

Figure 26a shows a decay muon radial distribution with a peak near 20 mm and a large low-side tail that arises from the non-ideal magnetic kicker pulses. The muons rotate in x-x'-phase space about different x_e, e.g. $\delta = 0\,\%$ (magic momentum) muons rotate around $x \approx 0$ mm and $\delta = 0.125\,\%$ muons with a quadrupole high voltage at 18.3 kV will rotate around $x \approx 9.96$ mm. *[Update with Run-2 based value]* Hence, the "wide-asymmetric" distribution completes one revolution in x-x'-phase space per 360° betatron phase advance, and so f_x is the dominant frequency of the radial width modulation. Figure 26b shows a Gaussian-like decay muon vertical distribution with a peak near 0 mm. The muon distribution mean and peak are near the y-y'-phase space origin, and so the "narrow-symmetric" distribution completes

Preliminary DRAFT Preliminary

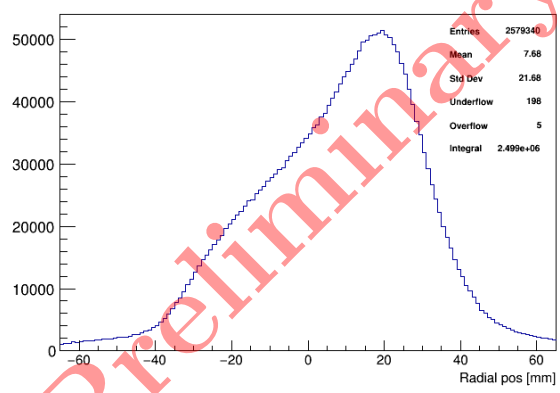

(a) Horizontal (radial) distribution.

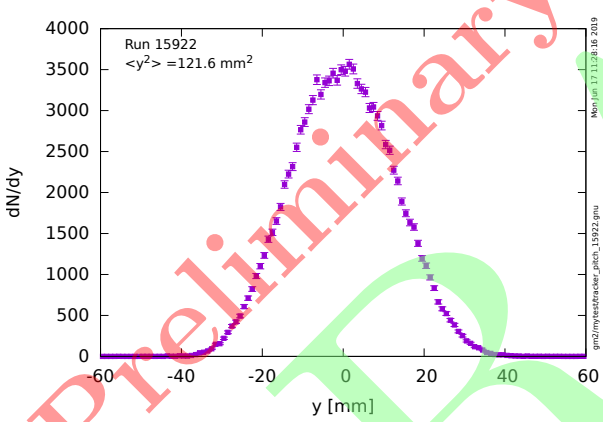

(b) Vertical distribution.

FIG. 26: David R. Decay muon distributions measured by the ?? straw tracker station for a subset of preliminary Run-1 data. The data is not corrected for acceptance or resolution. *Should the y-axis label read dN/dy or counts; remove timestamp and directory information; check with tracker experts.*

one revolution in phase space per 180° betatron phase advance. Hence, $2f_y$ is the dominant frequency of the vertical width modulation.

Muon bunches are injected into the storage ring and the bunches have a cyclotron motion with characteristic frequency f_c, where the longitudinal bunch width increases over time (debunching) due to the muon momentum spread. The coherent motion of the beam centroid and width are characterized by decoherence times. The coherent motion and modulation at early times is evident in Figs. 4 and 5 and decoherence at later times in Fig. 6. The beam decoheres in part due to the amplitude and momentum dependence of the tunes associated with the quadrupole nonlinearities, see Section V, and the chromaticity. But, the leading source of decoherence is the large momentum spread and the strong dependence of path length on momentum. The relative change in circumference is given by

$$\frac{\Delta C}{C_0} \approx \frac{\eta_x}{R_0}\delta \approx \delta$$

in the weak focusing limit, where ΔC is change in circumference, C_0 is the design orbit (magic) circumference, and the storage ring momentum acceptance is $\delta \sim \pm 0.125\,\%$. The distribution will lap itself in as few as 400 turns ($\sim$60 µs), effectively mixing the distribution. Indeed, a measure of the decoherence time is an indication of the momentum distribution width.

The detectors are at fixed locations and provide finite coverage around the storage ring, and so the cyclotron motion of the muon bunches creates an effective sample rate. The Nyquist frequency for the detectors is given by $f_c/2$. The f_x and $2f_y$ frequencies are larger than the Nyquist frequency, and so the data contains the corresponding Coherent Betatron Oscillation (CBO) and Vertical Waist (VW) alias frequencies respectively. The CBO and VW frequencies are physical alias frequencies, as they arise from the cyclotron motion and detector acceptance effects (an example of the the stroboscopic effect), as opposed to alias frequencies that can arise from histogram binning and associated discrete Fourier transforms. Table V gives important beam frequencies that affect the Run-1 data that was taken at the 18.3 kV EQS storage set-point.

Equation (3) is used to describe the decay positron time spectra after applying a suitable energy threshold cut to the positron events, where the Run-1 data is expected to have a N (normalization) dependance on the CBO and VW frequencies, A (asymmetry) dependance on the CBO frequency, and ϕ ($g-2$ phase) dependance on the CBO frequency. The normalization dependence on coherent beam motion is due to detector acceptance, as the likelihood of a positron striking a detector depends on the muon decay position. The asymmetry dependence on coherent beam motion is due to the modulation of the average detected positron energy, as there is a positron energy and muon decay position correlation for detected positrons. A detector does not measure the muon decay time, but the positron arrival time at the detector. The difference in times corresponds to a shift in the g–2 phase. Hence, the $g-2$ phase dependence on coherent beam motion is due to the detected positron time of flight, as there is a positron trajectory and muon decay position correlation for detected positrons.

Figure 27 shows CBO and VW effects in the frequency

Preliminary
Preliminary
DRAFT

TABLE V: Jason Important beam frequencies that affect the Run-1 decay positron spectra for the 18.3 kV EQS storage set-point *[Update with Run-2 based values]*. The tune values used to calculate the frequencies are taken from Table III.

Frequency	Variable	Expression	Value [MHz]	Corresponding Period [µs]
Anomalous Precession	f_a	$(ea_\mu B_0)/(2\pi m_\mu)$	0.2291	4.365
Cyclotron	f_c	$p_0/(2\pi m_\mu \gamma_0 R_0)$	6.705	0.1491
Horizontal Betatron	f_x	$\nu_x f_c$	6.334	0.1579
Vertical Betatron	f_y	$\nu_y f_c$	2.201	0.4543
Coherent Betatron Oscillation	$f_{\rm cbo}$	$f_c - f_x$	0.371	2.70
Vertical Waist	$f_{\rm vw}$	$f_c - 2f_y$	2.303	0.4342

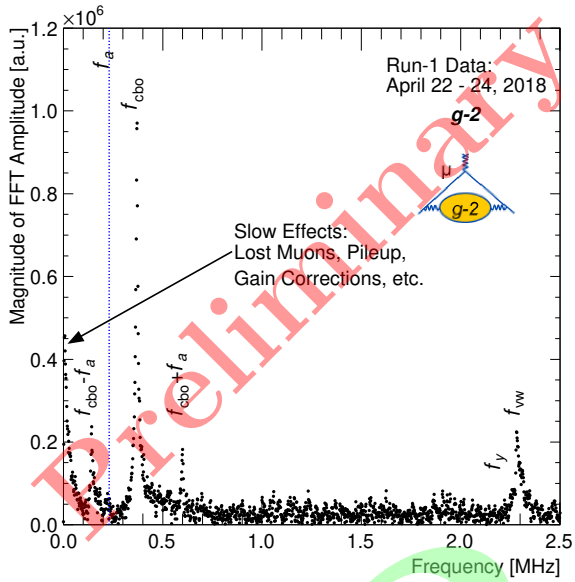

FIG. 27: Jason The Fast Fourier transform (FFT) frequency spectrum for 5-parameter fit residuals from a decay positron time spectrum. Specifically, the magnitude of the FFT amplitude is shown. This subset of Run-1 data was taken at $V_Q = 18.3\,\text{kV}$. *Final unless David S. wants to make an updated version.*

spectrum for fit residual from a decay positron time spectrum. A so called "5-parameter fit" is used to generate the fit residuals for Fig. 27, where the 5-parameter fit sets each of the N, A, and ϕ terms to a single fit parameter (constant function). The subset of Run-1 data used to produce Fig. 27 is probably too small to show the vertical betatron and twice CBO frequency effects, as these effects are expected to be very small [3].

A typical decay positron time spectrum fit function for the BNL level of statistics is given by Eq. 3 with

$$
\begin{aligned}
N(t) &= N_0 N_{\rm cbo}(t)\, N_{\rm vw}(t)\, \Lambda(t)\,, \\
N_{\rm cbo}(t) &= 1 + A^N_{\rm cbo} e^{-t/\tau_{\rm cbo}} \cos\left(\omega_{\rm cbo} t + \phi^N_{\rm cbo}\right), \\
N_{\rm vw}(t) &= 1 + A^N_{\rm vw} e^{-t/\tau_{\rm vw}} \cos\left(\omega_{\rm vw} t + \phi^N_{\rm vw}\right), \\
\Lambda(t) &= 1 - \kappa_{\rm loss} \int_0^t dt'\, e^{t'/\tau}\, L(t')\,, \\
A(t) &= A_0 \left[1 + A^A_{\rm cbo} e^{-t/\tau_{\rm cbo}} \cos\left(\omega_{\rm cbo} t + \phi^A_{\rm cbo}\right)\right], \\
\phi(t) &= \phi_0 + A^\phi_{\rm cbo} e^{-t/\tau_{\rm cbo}} \cos\left(\omega_{\rm cbo} t + \phi^\phi_{\rm cbo}\right). \qquad (20)
\end{aligned}
$$

The Λ term in Eq. (20) is used to model the muon exponential decay correction that arises from the so called "lost muons", which are lost during the measurement period due to beam interactions with storage ring materials. The Λ function is written in terms of the muon loss per lab frame lifetime function (L), which is determined by measuring the coincident minimum ionizing particles (MIPs) in the calorimeters that are produced by lost muons, see Section VI F. The $\kappa_{\rm loss}$ fit parameter gives the absolute scale of the muon losses after applying calorimeter gain and positron event pileup corrections. The N_0, $A_0 \sim 0.37$, and ϕ_0 fit parameters give the underlying normalization, asymmetry, and $g-2$ phase respectively. The CBO and VW decoherence are modeled by exponential terms with characteristic time constants $\tau_{\rm cbo}{\sim}180\,\mu$s and $\tau_{\rm vw}{\sim}20\,\mu$s respectively. The $A^N_{\rm cbo} \sim 0.004$, $A^A_{\rm cbo} \sim 0.0007$, and $A^\phi_{\rm cbo} \sim 0.0004$ fit parameters give the amplitudes and $\phi^N_{\rm cbo}$, $\phi^A_{\rm cbo}$, and $\phi^\phi_{\rm cbo}$ fit parameters give the corresponding phases of the CBO modulations, while the $A^N_{\rm vw} \sim 0.003$ fit parameter gives the amplitude and $\phi^N_{\rm vw}$ fit parameter gives the corresponding phase of the VW modulation. The $\omega_{\rm vw} \sim 14.4\,\text{rad}/\mu\text{s}$ fit parameter gives the angular frequency of the VW modulation *[check values]*.

The $\omega_{\rm cbo}$ fit parameter gives the angular frequency of the CBO modulation. Several of the EQS potted resistors, which are used to set the RC time constant for the transition from beam scraping to stable storage, were found to be damaged/defective after the completion of Run-1. The damage caused the effective resistance to be larger than expected, where two of the resistors have an RC time constant that is significantly larger than the

Preliminary
DRAFT

nominal 5 µs. This causes the ω_{cbo} to drift during the measurement period for the Run-1 data. A phenomenological model based on straw tracker data has been developed to model the ω_{cbo} drift for the Run-1 decay positron fit functions, which is given by

$$\omega_{\text{cbo}} = \omega_0 \left(1 + \Delta\omega t + T_1 e^{-t/\tau_1} + T_2 e^{-t/\tau_2}\right), \quad (21)$$

where $\omega_0 \sim 2.31\,\text{rad}/\mu\text{s}$, $\Delta\omega \sim 1.9 \times 10^{-5}/\mu\text{s}$, $T_1 \sim -0.051$, $\tau_1 \sim 73\,\mu\text{s}$, $T_2 \sim -0.13$, and $\tau_2 \sim 17\,\mu\text{s}$ *[check values; include 9-day and end-game models]*. The numerical values given for the Eqs. (20) and (21) fit parameters are for a subset of Run-1 data taken at the 18.3 kV EQS storage set-point, where the data from all of the calorimeters has been added together. The damaged potted resistors have been replaced with properly functioning resistors for Run-2 data collection, and so ω_{cbo} should be able to be treated as a single fit parameter (constant function) for Run-2.

The Fermilab experiment has the goal of collecting 20 times the total statistics collected by BNL (8.6348×10^9 decay positrons and electrons [3]). The increased statics may lead to the detection of small, as of yet unseen, coherent beam motion effects. The Eq. (20) CBO models are based on the radial modulation of the beam centroid, but detector acceptance effects may lead to the N, A, and ϕ terms having small dependences on higher-order moments of the beam. The N, A, and ϕ can be parametrized in terms of the decay muon phase space (x, x', y, y', s, $\dot{s}$, and t, where $\dot{s} \equiv ds/dt$) for each individual detector. The primary concern for the Fermilab experiment at full statistics is small effects from higher-order radial beam moments, and so the following discussion will only consider a dependance of N, A, and ϕ on x and x'. Furthermore, the problem will be simplified by only considering an explicit dependence on x, as x and x' are coupled variables, i.e. muon radial motion is described at leading-order by simple harmonic motion in x-x'-phase space.

Assume that the instantaneous dependence of the N, A, and ϕ terms on x for an individual detector may be expressed as Taylor series given by

$$\begin{aligned} N_I(x) &= \sum_{i=0}^{\infty} a_i (x-d)^i, \\ A_I(x) &= \sum_{i=0}^{\infty} b_i (x-d)^i, \\ \phi_I(x) &= \sum_{i=0}^{\infty} c_i (x-d)^i. \end{aligned} \quad (22)$$

The a_i, b_i, and c_i series coefficients depend on the d expansion point and E_{th}. The Eq. (22) coefficients are effective parameters that also depend on the integration of the decay muon distribution over the x', y, y', s, $\dot{s}$, and t variables, and these coefficients correspond to detector acceptance effects. Non-zero higher order terms ($i \geq 2$) can arise from the interaction of decay positrons with storage ring materials, e.g. kicker and quadrupole plates.

The time dependent decay muon moments with respect to d can be written as

$$\begin{aligned} \mu_i^d(t) &= \int_{-\infty}^{\infty} dx\, (x-d)^i \frac{\mathcal{B}(x,t)}{\mathcal{B}(t)}, \\ \int_0^{\infty} dt \int_{-\infty}^{\infty} dx\, \mathcal{B}(x,t) &= 1, \\ \mathcal{B}(t) &= \int_{-\infty}^{\infty} dx\, \mathcal{B}(x,t), \end{aligned} \quad (23)$$

where $\mathcal{B}(x,t)$ is a joint, $\mathcal{B}(t)$ is a marginal, and $\mathcal{B}(x,t)/\mathcal{B}(t)$ is a conditional probability density function (PDF) for the decay muons ($\mathcal{B}$ dependence on the x', y, y', s, and $\dot{s}$ variables has been integrated and normalized away) *[check statistics lingo]*. The simplest way to think about this problem is to use $d = 0$ (raw moments), but the raw moments can be written in terms of the mean and central moments via Eq. (23) by letting d be equal to the time dependent mean and expanding out the $(x-d)^i$ term into a finite Maclaurin series before carrying out the integration. The generic form of the final fit function models should not matter on whether raw or central moments are used, as both types of moments should lead to a collection of equilibrium terms and periodic terms that decay away.

Equations (23) and (22) can then be used to write N, A, and ϕ as functions of t:

$$\begin{aligned} N(t) &= \int_{-\infty}^{\infty} dx\, N_I(x) \frac{\mathcal{B}(x,t)}{\mathcal{B}(t)} = a_0 + \sum_{i=1}^{\infty} a_i \mu_i^d(t), \\ A(t) &= \int_{-\infty}^{\infty} dx\, A_I(x) \frac{\mathcal{B}(x,t)}{\mathcal{B}(t)} = b_0 + \sum_{i=1}^{\infty} b_i \mu_i^d(t), \\ \phi(t) &= \int_{-\infty}^{\infty} dx\, \phi_I(x) \frac{\mathcal{B}(x,t)}{\mathcal{B}(t)} = c_0 + \sum_{i=1}^{\infty} c_i \mu_i^d(t). \end{aligned} \quad (24)$$

The $\mu_0^d(t) = 1$ by construction, but the $i \geq 1$ decay muon moments are expected to have the form of an equilibrium term added to a periodic (modulation) term that decays away (decoheres), because the muons spread out and fill up the storage ring admittance as the beam motion decoheres over the measurement period due to nonlinear effects. The $i \geq 1$ decay muon moments in Eqs. (23) and (24) can be written as

$$\begin{aligned} \mu_i^d(t) = E_i^d(t) + \\ D_i^d(t) \left[A_{i,0}^d + \sum_{j=1}^{\infty} A_{i,j}^d \cos\left(j\omega_{\text{cbo}} t + \phi_{i,j}^d\right) \right], \end{aligned} \quad (25)$$

where $E_i^d(t)$ is the equilibrium term, $D_i^d(t)$ is the decay envelope, and the cosine Fourier series inside of the brackets is the periodic term. The BNL fit model given in Eq. (20) only considers the $i \leq 1$ and $j \leq 1$ case

DRAFT

for Eqs. (24) and (25), where $E_1^d(t)$ = constant value, $D_1^d(t) = \exp(-t/\tau_{\rm cbo})$, and $A_{1,0}^d = 0$. Furthermore, the $\phi_{1,1}^d$ is treated as a separate fit parameter for each of the N, A, ϕ terms, because the corresponding cosine amplitude and phase fit parameters are correlated at some level and the different cosine amplitude fit parameters are neither equal to $A_{1,1}^d$ nor each other. The $D_1^d(t) = \exp(-t/\tau_{\rm cbo})$ model in particular and the fit model as a whole are not expected to be perfectly accurate, and letting the $\phi_{1,1}^d$ be a separate fit parameter for each of the N, A, ϕ terms allows the fit function to be more "flexible with the data".

The BNL model can be used to fit data from individual detectors or a collection of detectors, where the CBO effects are significantly reduced if the positron data from all of the calorimeters is added together. The reduction in CBO effects occurs because the CBO modulations are 180° out of phase for the detectors that are on opposite sides of the storage ring. Perfect cancellation does not occur because the detectors are not perfectly aligned and they have different decay positron acceptances. The BNL fit model uses the same decohrence model for the N, A, and ϕ terms, but this may not be adequate for the full Fermilab statistics. Furthermore, new decohrence models may need to be developed given the different individual detector acceptances and potential contributions from higher order beam moments.

B. Pitch Correction

David R.

Our measurement of the anomalous precession frequency of the muon depends on the correlation of muon velocity and muon polarization. The projection of polarization onto velocity is given by (Jackson 11.171)

$$\frac{d}{dt}(\hat{\beta}\cdot\mathbf{s}) = -\frac{e}{mc}\mathbf{s}_\perp\cdot\left[a_\mu(\hat{\beta}\times\mathbf{B}) + \left(a_\mu - \frac{1}{\gamma^2-1}\right)\beta\mathbf{E}\right]. \tag{26}$$

The dependence of ω_a on the amplitude of vertical betatron oscillations appears in the term $\hat{\beta}\times\mathbf{B}$ in Eq. (26). If $\mathbf{B} = B\hat{\mathbf{y}}$ and $\hat{\beta} = \sin\psi_{yz}\hat{\mathbf{y}} + \cos\psi_{yz}\hat{\mathbf{z}}$ then $\hat{\beta}\times\mathbf{B} \sim \beta_z B = \beta(\cos\psi_{yz})B$, where ψ_{yz} is the angle of the trajectory in the $y-z$ plane. The contribution to ω_a due to the pitch for a particular trajectory is $\frac{\Delta\omega_a}{\omega_a} = (1-\cos\psi_{yz})$ and for $\psi_{yz} \ll 1$,

$$\frac{\Delta\omega_a}{\omega_a} \sim \frac{1}{2}\psi_{yz}^2.$$

The contribution from the pitch angle averaged over all ϕ for each amplitude a and then over all possible amplitudes a, is

$$\langle\langle\frac{\Delta\omega_a}{\omega_a}\rangle_\phi\rangle_a \sim \frac{1}{2}\langle\langle\psi_{yz}^2\rangle_\phi\rangle_a.$$

In the limit of strictly linear betatron motion, the displacement y is related to amplitude a according to $y = \sqrt{a\beta_y}\cos\phi_y$, where ϕ_y is the betatron phase advance. Then the angle

$$\psi_{yz} = \psi_0\sin\phi = \sqrt{\frac{a}{\beta_y}}\sin\phi_y.$$

The average of ψ_{yz}^2 over all ϕ_y for amplitude a is

$$\langle\psi_{yz}^2(a)\rangle_\phi = \frac{1}{2}\psi_0^2(a) = \frac{\langle y^2(a)\rangle_\phi}{\beta^2}.$$

Next, average over all amplitudes a. We suppose that the distribution of amplitudes is given by some function $P(a)$ defined over the physical aperture. Then

$$\langle\langle y^2\rangle_\phi\rangle_a = \frac{1}{2}\beta\frac{\int_{aper} aP(a)da}{\int_{aper} P(a)da}$$

$$\langle\langle\psi^2\rangle_\phi\rangle_a = \frac{1}{2}\langle\psi_0^2\rangle_a = \frac{a}{\beta^2}\langle\langle y^2\rangle_\phi\rangle_a$$

$$C_p \equiv \frac{\Delta\omega_a}{\omega_a} = \frac{1}{4}\langle\psi_0^2\rangle_a = -\frac{n\langle y^2\rangle}{2R_0^2},$$

where $\beta_y = \frac{\sqrt{n}}{R_0}$.

The vertical distribution of decay positrons is measured by the straw tracking chambers. Tracks of positrons are extrapolated back to the parent muon decay point to determine the vertical distribution of the muons as shown for a subset of the data in Fig. 26b.

C. E-field Correction

David R.

The E-field systematic is associated with the third term on the right hand size of Eq. (4) and depends on momentum and radial electric field. The contribution from the electric field is minimized by operating near the magic momentum, namely where $a_\mu = \frac{1}{\gamma^2-1}$. The field of the ring magnet is chosen so that the closed orbit of the magic momentum muon corresponds to the design trajectory. Then the contribution to ω_a is

$$C_e \sim -2\frac{\Delta p}{p_m}\frac{\vec{\beta}\times\vec{E}}{Bc}, \tag{27}$$

where p_m is the magic momentum γ and β are evaluated at p_m.

The electric field depends on transverse displacement in the quadrupoles. Insofar as the field is with displacement, the average electric field along the trajectory is proportional to the average radial displacement x_e, namely the closed orbit. The average radial electric field is given by

$$\langle E_r\rangle = n\left(\frac{v_s B}{R_0}\right)x_e,$$

DRAFT

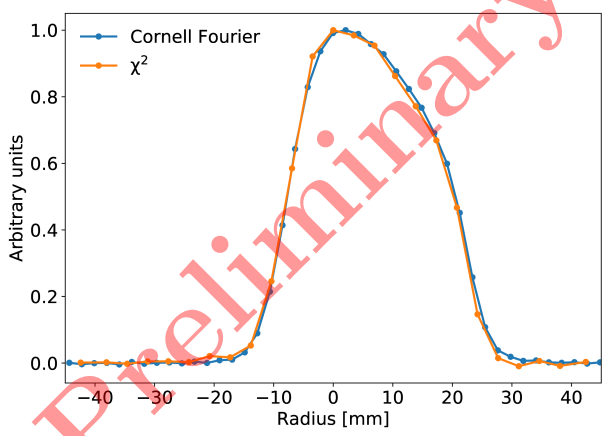

FIG. 28: David R. Fourier analysis of the fast rotation signal and parameterized fit give the muon equilibrium radial (closed orbit) distribution revolution. *Harmonize notation; do we want lines connecting the points.*

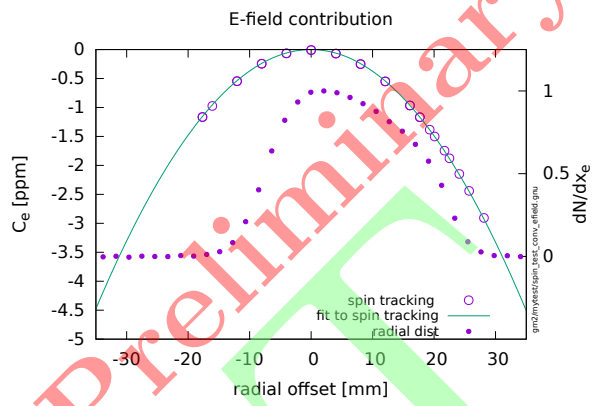

FIG. 29: David R. The contribution to ω_a (C_e) due to the electric field is computed by spin tracking as a function of muon momentum and plotted in terms of the closed orbit. The measured radial distribution is superimposed. The average correction is the convolution of the two. *Harmonize notation; should right-side y-axis label read dN/dx_e or counts; should x-axis range go from ± 45 mm.*

where n is the focusing index. The average radial displacement is

$$x_e = \eta \frac{\Delta p}{p}.$$

Then the contribution to ω_a due to electric field is

$$C_e \sim -2\beta^2 n(1-n)\frac{x_e^2}{R_0^2},$$

where $\eta =\sim \frac{1-n}{R_0}$. Determination of the E-field correction thus depends on measurement of the equilibrium radial distribution. (The magnitude of the E-field correction is reduced by a few percent due to the nonlinearity of the quadrupole field.)

The radial distribution is determined by a "fast rotation analysis", that exploits the connection between the revolution frequency and the radial displacement. A technique [28] based on Fourier transform yields a frequency spectrum that can be correlated with radius (circumference) and momentum. An alternative method extracts the radial distribution from the measured debunching of the muon beam. The fast rotation data is provided by the calorimeters which measure the time dependence of the intensity of the distribution. An example of radial (closed orbit) distribution extracted by both the Fourier method and the debunching analysis are shown in Fig. 28. The dependence of the E-field contribution to ω_a, on the radial offset of the closed orbit, superimposed on the the measured distribution is shown in Fig. 29.

D. Spin Correlations & Early-to-late Effects

Jason

The total spin phase (argument) of the cosine function in Eq. (3) can be written in the following general form:

$$\Phi(t) = \left[\int_0^t dt'\,\omega_a(t')\right] + \phi(t). \tag{28}$$

The difference between Eqs. (3) and (28) is that ω_a is allowed to be a function of time. For example, ω_a will become time dependent if the magnetic or electric fields are changing with time during the measurement period. Equation (28) illustrates the ambiguity between the ω_a and ϕ in a fit, where the ω_a and ϕ fit terms are treated as constant values under ideal conditions without experimental systematic effects. The Φ is the quantity being measured, while the ω_a and ϕ require accurate models to precisely extract the ω_a due to muon precession. There will be a shift in the constant ω_a fit value if the fit function does not accurately model the time dependence of ϕ. This can be illustrated by expanding ϕ into a Maclaurin series,

$$\phi(t) = \phi(0) + \frac{d\phi(0)}{dt}t + \frac{1}{2}\frac{d^2\phi(0)}{dt^2}t^2 + \cdots,$$

and noting that the linear term has the same functional form as the $\omega_a t$ term in Eq. (3).

Preliminary
Preliminary
DRAFT

The combination of spin correlations and corresponding so called "early-to-late effects" form an important class of systematic effects that need to be considered. In this context, a decay muon property F (e.g. x, y, p, etc.) is said to have correlations with spin if

$$\frac{\partial \phi_0}{\partial \langle F \rangle} \neq 0,$$

where $\langle F \rangle$ is the mean value of the decay muon property F and ϕ_0 is the "constant" component of the $g-2$ phase. The ϕ_0 is modeled as a constant fit parameter, which is added to the temporal modulation of ϕ due to the coherent beam motion, e.g. see Eq. (20). Furthermore, the decay muon property F is said to have early-to-late effects if

$$\frac{d\langle F \rangle}{dt} \neq 0.$$

If spin correlations and corresponding early-to-late effects combine together, then this implies that ϕ_0 is really a function of time, since

$$\frac{d}{dt}\phi_0\left(\langle F \rangle(t), \langle G \rangle(t), \langle H \rangle(t), \cdots\right) = \frac{\partial \phi_0}{\partial \langle F \rangle}\frac{d\langle F \rangle}{dt} + \frac{\partial \phi_0}{\partial \langle G \rangle}\frac{d\langle G \rangle}{dt} + \frac{\partial \phi_0}{\partial \langle H \rangle}\frac{d\langle H \rangle}{dt} + \cdots \neq 0, \tag{29}$$

where $F, G, H, \cdots$ are decay muon properties and the equality is obtained from the chain rule for multivariable functions with one independent variable. *Double check chain rule!* The dependence of ϕ_0 on $\langle F \rangle, \langle G \rangle, \langle H \rangle, \cdots$ can be obtained from a decay positron fit over a very small time window centered on time t for each corresponding set of $\langle F \rangle, \langle G \rangle, \langle H \rangle, \cdots$ values at time t. The decay positron fit function is assumed to accurately model the ω_a term, because the ω_a and ϕ terms are coupled in the fit as indicated by Eq. (28). The $\langle F \rangle, \langle G \rangle, \langle H \rangle, \cdots$ values at time t can be obtained by taking the mean of the $F, G, H, \cdots$ values in the very small time window centered on time t.

Nonuniform spin-momentum distributions are generated in the Muon Campus beamline and muon storage ring, which will then produce spin-momentum correlations,

$$\frac{\partial \phi_0}{\partial \langle p \rangle} \neq 0,$$

in the muon storage ring. The majority of the muons are produced from pion decays in the M2-line and M3-line, which are primarily straight sections that transport positive pions and collect decay muons. The M2-line and M3-line FODO cells (alternating focusing and defocusing magnets) and dipole bending magnets will generate some spin-momentum distribution for the muons produced in these sections of the Muon Campus. In particular, a dipole bending magnet will change the angle between the muon spin and momentum by

$$\Delta\phi_{sp} \approx a_\mu \gamma \phi_b, \tag{30}$$

where ϕ_b is the angle at which the muon bends through the dipole field. Equation (30) indicates that dipole bending magnets will lead to nonuniform spin-momentum distributions, as the Lorentz factor can be written as a function of momentum:

$$\gamma = \sqrt{1 + \left(\frac{p}{m_\mu c}\right)^2}.$$

The initial decay muon transverse component of spin, x', and y' all depend on the direction of the initial muon momentum when the pion decays. A FODO cell maximum x-x' admittance and y-y' admittance occur at the horizontal-defocusing-vertical-focusing and horizontal-focusing-vertical-defocusing magnets respectively. Thus, most of the muons with a large horizontal spin component come from pion decays near the horizontal-defocusing-vertical-focusing magnets, and most muons with a large vertical spin component come from pion decays near the horizontal-focusing-vertical-defocusing magnets. The dependence between spin and the transverse coordinates decreases as the distance between the magnets decreases, which creates smaller β functions. The dependence of the muon storage ring x_e on p and the use of circular collimators in the muon storage ring leads to a dependance of x, x', y, and y' on p. Hence, the FODO cells will also lead to nonuniform spin-momentum distributions.

Some of the muons are also produced from kaon and pion decays that occur before the beam reaches the M2-line. A momentum spectrometer is used to inject the $\sim$3.1 GeV/c positive particles from the Inconel-600 target into the M2-line. The momentum spectrometer is composed of the pulsed dipole magnet (PMAG), water-cooled collimator that protects the PMAG, and beam dump for the off-momentum particles. Some of the muons that are produced before and inside of the spectrometer will have a momentum that is $\sim$3.1 GeV/c, and so they will be injected into the M2-line. These so called "target muons" will have a different spin-momentum distribution than the muons from the M2-line and M3-line, as the target muons are produced and collected under different conditions.

Muons are also produced from pion decays in the Delivery Ring (DR). The DR is a storage ring that is used to remove the proton contamination from the beam and to provide time for the remaining pions to decay into muons. The spin tune for a storage ring with a dipole magnetic field is given by

$$\begin{aligned} \omega_c &= \frac{1}{\gamma}\frac{qB}{m}, \\ \omega_a &\approx a_\mu \frac{qB}{m}, \\ \nu_a &= \frac{\omega_a}{\omega_c} \approx a_\mu \gamma, \end{aligned} \tag{31}$$

where ω_c is the cyclotron frequency, ω_a is the anomalous precession frequency, and B is the magnitude of the

DRAFT

dipole magnetic field. Equation (30) can be derived from Eq. (31), because one can imagine a dipole bending magnet as being a component in some storage ring (charged particles travel in circular arcs). The DR is made out of FODO cells and bending dipole magnets, and so the muons on the design orbit should only experience the net bending field. Thus, the approximation given in Eq. (30) is valid for the DR, where the angle between the muon spin and momentum changes by

$$\Delta\phi_{sp} = \nu_a \phi_b \approx a_\mu \gamma \phi_b = 2\pi a_\mu \gamma M, \tag{32}$$

where M is the number of turns the muon has gone around the storage ring, and the γ dependence on p will lead to nonuniform spin-momentum distributions. The DR is expected to affect the spin-momentum distribution somewhere around the mrad level, as Eq. (32) leads to $\Delta\phi_{sp} \approx 0.214\,669\,\mathrm{rad}$ per 1 turn for $\delta = 0\,\%$ and $\Delta\phi_{sp} \approx 0.214\,937\,\mathrm{rad}$ per 1 turn for $\delta = 0.125\,\%$, where $a_\mu \approx 0.001\,165\,92$, $m \approx 0.105\,658\,\mathrm{GeV}/c^2$, and $p_0 \approx 3.094\,35\,\mathrm{GeV}/c$ *Check arithmetic*. The muon campus beam undergoes 4 turns around the DR for physics quality data before it is extracted and sent to the muon storage ring. The so called "DR muons" will have a different spin-momentum distribution than the other muons, as the DR muons are produced and collected under different conditions than the other muons. Figure 30 gives estimated spin x- and y-component distributions for muons born in the M2-line, M3-line, and DR.

There is also a nonuniform spin-momentum distribution that arises from the muon storage ring beam injection and kick, which is negligible for the BNL level of statistics, but should be studied for the full Fermilab experiment statistics. The muon bunches extend along the longitudinal direction ($\sim$150 ns full bunch width), where the muons at the head of the bunch have spent more time precessing in the storage ring magnetic field than the muons at the tail of the bunch. Thus, the beam injection leads to a gradient in Δ_{sp} across the longitudinal bunch length. The storage ring Kicker System magnetic field is nonuniform over the longitudinal length of the bunch, and the muon momentum acceptance depends on the integrated Kicker field seen by a muon. Thus, the beam kick leads to a gradient in p across the longitudinal bunch length. Hence, there is nonuniform spin-momentum distribution that depends on the longitudinal position across a bunch.

The average $\Delta\phi_{sp}$ per time interval Δt in the storage ring depends on the muon trajectories, as a muon trajectory will determine what magnetic and electric fields are seen by the muon. Since x_e depends on p, then a trajectory also depends on p. There are two equivalent toy models that can be used to determine the average $\Delta\phi_{sp}$ per Δt. One could assume that there is a time independent ω_a and time dependent initial phase ϕ_0. One could instead assume that there is a time dependent ω_a and time independent ϕ_0. These two models are both consistent with Eq. (28). This leads to the question of how one should classify the different spin-momentum based effects. The convention that has arisen over time is that a nonuniform spin-momentum distribution is considered to affect ϕ_0 when the distribution is created before the decay positron fit start time ($\sim$30 µs after beam injection into the ring), and the distribution is consider to affect ω_a when it is created during the fit time window, e.g. the E-field and pitch corrections.

The lost muon spin systematic effect is significant for the Run-1 dataset, where it arises from the spin-momentum correlation due to the nonuniform spin-momentum distributions discussed in this section and the lost muon early-to-late effect,

$$\frac{d\langle p\rangle}{dt} \neq 0,$$

which is caused by the loss of muons during the measurement period, see Section VI F for more details. There is also the differential decay early-to-late effect,

$$\frac{d\langle p\rangle}{dt} \neq 0,$$

which is caused by the muon lab-frame lifetime dependence on γ, where γ is in turn dependent on p. The nonuniform spin-momentum distributions discussed in this section also couple with the differential decay early-to-late effect, which is negligible for the BNL level of statistics, but should be studied for the full Fermilab Experiment statistics.

E. Spin Resonances

Jason

Blah blah blah ....

F. Lost Muons

Sudeshna

During the first couple of hundred turns after injection, muons outside the aperture defined by the collimators are scraped out, and ideally particles that survive scraping will be lost only to decay. There may however be some particles with long time scale unstable motion, perhaps associated with a resonance (Fig. 31), that eventually exit. Particles may also be lost to scattering from residual gas. If there is any correlation of these lost muons with the parameters of the muon phase space, the distribution will change with time and confuse our corrections. If the lost muons populate a portion of the phase space that is correlated with momentum or position, the phase space of muons contributing to the measurement of polarization will be distorted. the difference frequency will change as the lost particles are lost.

The phase space volume of the injected muon distribution overwhelms the ring acceptance. As a result, the

DRAFT

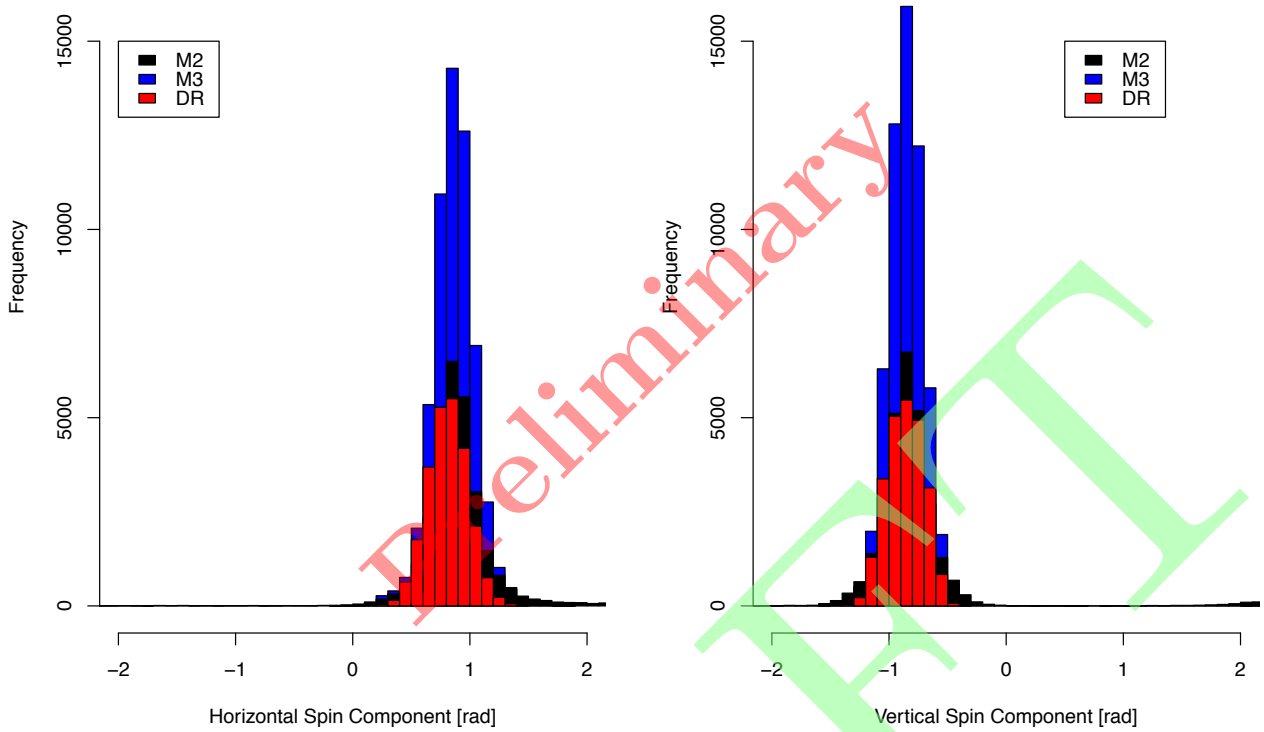

FIG. 30: Mike Horizontal and vertical muon spin component distributions near the entrance to the Storage Ring for $\sim 10^5$ muons born in the Muon Campus M2-line, M3-line, and Delivery Ring (DR). These distributions have been generated using the G4beamline model of the Muon Campus lattice. *Harmonize notation; do the spin units make sense.*

Preliminary
DRAFT

distribution that is stored fills the aperture. Muons at the edge of the momentum or transverse aperture may be lost over the course of a fill. If those losses correlate with any particular region of the muon phase space or polarization, there will be a systematic distortion on the measurement of momentum and/or phase space distribution and/or ω_a phase [**?**]. If for example, high momentum muons are lost early in the fill by hitting an aperture, there will be a systematic shift of the ω_a phase over the course of the fill as the lower momentum muons in the distribution decay away. Or if particles with large vertical oscillation are lost, the pitch correction can be skewed.

In order to insure that all circulating muons are well within the aperture defined by the collimators, muons at the edge of the aperture are scraped at the start of the fill. The scraping is accomplished by adjusting the voltages on the quadrupole plates asymmetrically, thereby introducing an electrostatic dipole moment, that displaces the closed orbit by about 2 mm both vertically and radially from the center of the aperture. The asymmetric voltages are sustained for 7 µs (many betatron periods) and then the closed orbit is restored adiabatically. The vertical displacement of the distribution is measured by the traceback detectors (see Fig. 32) at a point in the ring 180° beyond the injection point and over the course of the scraping cycle. The remaining distribution on the restored closed orbit will nominally have at least 1 mm clearance with respect to the collimators. Muons that are lost are identified as a double (or triple) coincidence in adjacent calorimeters so that the effectiveness of the scraping procedure can be confirmed.

VII. CONCLUSION

Jason

A quantitative understanding of the evolution of the muon distribution over the course of the fill is essential to limiting the systematic uncertainty in the measurement of the anomalous magnetic moment to the 70 ppb (systematic) target. The experiment is equipped with detectors that can measure phase space and momentum distribution in some detail, as we have demonstrated with a few examples. Beam dynamics simulations informed by the measurements complete the description. The preliminary data presented above was collected during the commissioning phase of the experiment. Nevertheless it is clear that the fiber harp and tracker systems are an extraordinary window on the behavior of the circulating distribution.

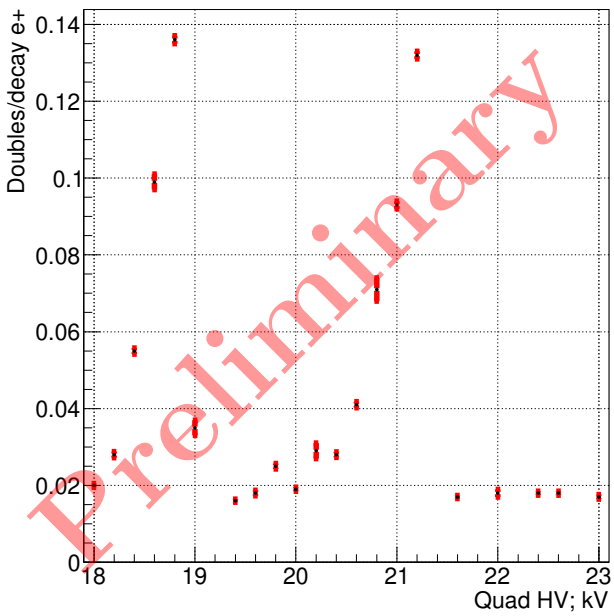

FIG. 31: Sudeshna Fraction of lost muons as a function of EQS storage set-point voltage for calorimeter 1. An increased lost muon rate is observed from the betatron resonances centered near 18.8 and 21.2 kV. These resonances are due to the $3\nu_y = 1$ and $\nu_x + 2\nu_y = 2$ lines in the tune plane. *Harmonize notation; update with Run-2 calo data; do we need to compare to Run-1 data; add COSY curve.*

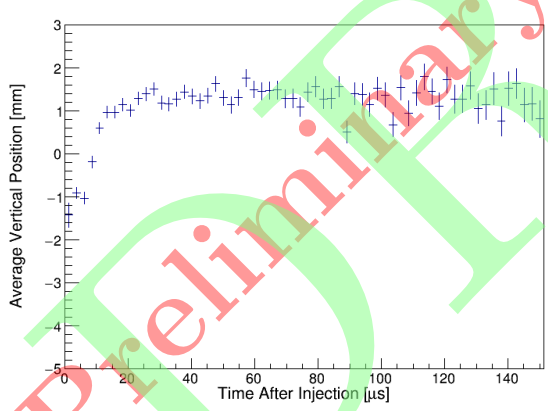

FIG. 32: David R. Vertical displacement of the centroid at the 180° tracker during the scraping cycle. *Check with tracker experts.*

ACKNOWLEDGMENTS

Jason

We thank E989 Collaborators, the Fermi National Accelerator Laboratory, a U.S. Department of Energy, Office of Science, HEP User Facility for the resources provided. Fermilab is managed by the Fermi Research Alliance, LLC(FRA), acting under Contract No. DE-AC02-07CH11359. The authors are supported by the US NSF, and the UK STFC. I also wish to thank all of our colleagues who made this experiment and these measurements possible and with whom I have benefited from countless discussions.

Appendix A: An Appendix

Jason

I am thinking about putting something in about calculating the field index (n) ....

1. An Appendix Subsection

Blah blah blah ....

DRAFT

[1] G. Charpak *et al.*, A New Measurement of the Anomalous Magnetic Moment of the Muon, Phys. Lett. **1**, 16 (1962).

[2] J. Bailey *et al.* (CERN-Mainz-Daresbury), Final Report on the CERN Muon Storage Ring Including the Anoma-

lous Magnetic Moment and the Electric Dipole Moment of the Muon, and a Direct Test of Relativistic Time Dilation, Nucl. Phys. **B150**, 1 (1979).

[3] G. W. Bennett *et al.* (Muon g-2), Final Report of the Muon E821 Anomalous Magnetic Moment Measurement at BNL, Phys. Rev. **D73**, 072003 (2006), arXiv:hep-ex/0602035 [hep-ex].

[4] G. W. Bennett *et al.* (Muon (g-2)), An Improved Limit on the Muon Electric Dipole Moment, Phys. Rev. **D80**, 052008 (2009), arXiv:0811.1207 [hep-ex].

[5] J. Grange *et al.* (Muon g-2), Muon (g-2) Technical Design Report, (2015), arXiv:1501.06858 [physics.ins-det].

[6] P. J. Mohr *et al.*, CODATA Recommended Values of the Fundamental Physical Constants: 2014, Rev. Mod. Phys. **88**, 035009 (2016), arXiv:1507.07956 [physics.atom-ph].

[7] M. Tanabashi *et al.* (Particle Data Group), Review of Particle Physics, Phys. Rev. **D98**, 030001 (2018).

[8] Fermilab Muon Department: Accelerator Division, `https://muon.fnal.gov`, (accessed: Aug. 8, 2019).

[9] D. Stratakis *et al.*, Accelerator performance analysis of the Fermilab Muon Campus, Phys. Rev. Accel. Beams **20**, 111003 (2017), arXiv:1803.00597 [physics.acc-ph].

[10] D. Stratakis *et al.*, Commissioning and first results of the Fermilab Muon Campus, Phys. Rev. Accel. Beams **22**, 011001 (2019).

[11] E. L. Hubbard *et al.*, Booster Synchrotron, FERMILAB-TM-0405 (1973).

[12] B. C. Brown *et al.*, The Fermilab Main Injector: high intensity operation and beam loss control, Phys. Rev. ST Accel. Beams **16**, 071001 (2013), arXiv:1307.2934 [physics.acc-ph].

[13] J. Morgan, Pbar Production Target Performance in Run II, FERMILAB-PBAR-NOTE-683 (2003).

[14] A. T. Fienberg *et al.*, Studies of an array of PbF_2 Cherenkov crystals with large-area SiPM readout, Nucl. Instrum. Meth. **A783**, 12 (2015), arXiv:1412.5525 [physics.ins-det].

[15] J. Kaspar *et al.*, Design and performance of SiPM-based readout of PbF_2 crystals for high-rate, precision timing applications, JINST **12** (01), P01009, arXiv:1611.03180 [physics.ins-det].

[16] R. Prigl *et al.*, A high precision magnetometer based on pulsed NMR, Nucl. Instrum. Meth. **A374**, 118 (1996).

[17] G. T. Danby *et al.*, The Brookhaven muon storage ring magnet, Nucl. Instrum. Meth. **A457**, 151 (2001).

[18] Y. K. Semertzidis *et al.*, The Brookhaven muon (g-2) storage ring high voltage quadrupoles, Nucl. Instrum. Meth. **A503**, 458 (2003).

[19] J. Crnkovic *et al.*, Commissioning the Muon g-2 Experiment Electrostatic Quadrupole System, in *Proc. 9th International Particle Accelerator Conference (IPAC'18), Vancouver, BC, Canada, April 29-May 4, 2018*, International Particle Accelerator Conference No. 9 (JACoW Publishing, Geneva, Switzerland, 2018) pp. 1848–1851.

[20] A. Yamamoto *et al.*, The superconducting inflector for the BNL g-2 experiment, Nucl. Instrum. Meth. **A491**, 23 (2002).

[21] N. Froemming *et al.*, Commissioning the Superconducting Magnetic Inflector System for the Muon g-2 Experiment, in *Proc. 9th International Particle Accelerator Conference (IPAC'18), Vancouver, BC, Canada, April 29-May 4, 2018*, International Particle Accelerator Conference No. 9 (JACoW Publishing, Geneva, Switzerland, 2018) pp. 1844–1847.

[22] A. Schreckenberger *et al.*, New Fast Kicker Results from the Muon g-2 E-989 Experiment at Fermilab, in *Proc. 9th International Particle Accelerator Conference (IPAC'18), Vancouver, BC, Canada, April 29-May 4, 2018*, International Particle Accelerator Conference No. 9 (JACoW Publishing, Geneva, Switzerland, 2018) pp. 4879–4881.

[23] G4beamline, `http://www.muonsinternal.com/muons3/G4beamline`, (accessed: Aug. 8, 2019).

[24] S. Agostinelli *et al.* (GEANT4), GEANT4: A Simulation toolkit, Nucl. Instrum. Meth. **A506**, 250 (2003).

[25] D. Sagan, Bmad: A relativistic charged particle simulation library, *Computational accelerator physics. Proceedings, 8th International Conference, ICAP 2004, St. Petersburg, Russia, June 29-July 2, 2004*, Nucl. Instrum. Meth. **A558**, 356 (2006).

[26] C. M. Poole *et al.*, A CAD Interface for GEANT4, (2011), arXiv:1105.0963 [physics.med-ph].

[27] C. M. Poole *et al.*, A CAD interface for GEANT4, Australas. Phys. Eng. Sci. Med. **35**, 329 (2012).

[28] Y. Orlov *et al.*, Muon revolution frequency distribution from a partial-time Fourier transform of the g-2 signal in the muon g-2 experiment, Nucl. Instrum. Meth. **A482**, 767 (2002).

DRAFT